Observations and Chemical Modeling of the Isotopologues of Formaldehyde and the Cations of Formyl and Protonated Formaldehyde in the Hot Molecular Core G331.512–0.103

Edgar Mendoza[1] , Miguel Carvajal[1,2] , Manuel Merello[3], Leonardo Bronfman[3] , and Heloisa M. Boechat-Roberty[4]

[1] Dept. Ciencias Integradas, Facultad de Ciencias Experimentales, Centro de Estudios Avanzados en Física, Matemática y Computación, Unidad Asociada GIFMAN, CSIC-UHU, Universidad de Huelva, Spain; edgar.mendoza@dci.uhu.es
[2] Instituto Universitario Carlos I de Física teórica y computacional, Universidad de Granada, Spain
[3] Departamento de Astronomía, Universidad de Chile, Casilla 36-D, Santiago de Chile, Chile
[4] Observatório do Valongo, Universidade Federal do Rio de Janeiro, Ladeira do Pedro Antônio, 43, Rio de Janeiro, RJ, Brazil

Abstract

In the interstellar cold gas, the chemistry of formaldehyde (H_2CO) can be essential to explain the formation of complex organic molecules. On this matter, the massive and energetic protostellar object G331 is still unexplored; hence, we carried out a comprehensive study of the isotopologues of H_2CO, the formyl cation (HCO^+), and protonated formaldehyde (H_2COH^+) through the APEX observations in a spectral window of $\sim$159–356 GHz. We employed observational and theoretical methods to derive the physical properties of the molecular gas combining LTE and non-LTE analyses. Formaldehyde was characterized via 35 lines of H_2CO, $H_2^{13}CO$, HDCO, and $H_2C^{18}O$. The formyl cation was detected via eight lines of HCO^+, $H^{13}CO^+$, $HC^{18}O^+$, and $HC^{17}O^+$. Deuterium was clearly detected via HDCO, whereas DCO^+ remained undetected. The H_2COH^+ was detected through three clean lines. According to the radiative analysis, formaldehyde appears to be embedded in a bulk gas with a wide range of temperatures ($T \sim$ 20–90 K), while HCO^+ and H_2COH^+ are primarily associated with colder gas ($T \lesssim 30$ K). The reaction $H_2CO + HCO^+ \rightarrow H_2COH^+ + CO$ is crucial for the balance of the three species. We used the Nautilus gas–grain code to predict the evolution of their molecular abundances relative to H_2; their values at timescales of $\sim 10^5$ yr matched the observations in G331: $[H_2CO] = (0.2–2) \times 10^{-8}$, $[HCO^+] = (0.5–4) \times 10^{-9}$, and $[H_2COH^+] = (0.2–2) \times 10^{-10}$. Based on the molecular evolution of H_2CO, HCO^+, and H_2COH^+, we hypothesized about the young lifetime of G331, which is consistent with the active gas–grain chemistry of massive protostellar objects.

Unified Astronomy Thesaurus concepts: Interstellar molecules (849); Astrochemistry (75); Molecular data (2259); Astronomy data analysis (1858); Spectral line identification (2073); Star forming regions (1565); Molecular reactions (2226)

1. Introduction

Formaldehyde was one of the first organic molecules detected in the interstellar medium (ISM; Snyder et al. 1969; Gardner & Whiteoak 1974). This compound has been observed in both the gas and solid phases of the ISM (Meier et al. 1993; Schutte et al. 1996; Féraud et al. 2019). Formaldehyde also plays a key role in the interstellar synthesis of prebiotic and complex organic molecules (Ferus et al. 2019; Layssac et al. 2020; Paiva et al. 2023).

In observational studies, Mangum et al. (1990) used maps and spectral lines of H_2CO to constrain the different components of the Orion Kleinmann–Low (KL) star-forming region, which has been largely discussed in the context of cold regions, hot cores and molecular outflows (Wootten et al. 1984; Sutton et al. 1995; Zapata et al. 2011). Pegues et al. (2020) analyzed maps of H_2CO toward a sample of disks surveyed with the Atacama Large Millimeter/submillimeter Array (ALMA). They highlighted the importance of H_2CO in understanding the production mechanisms of O-bearing molecules in disks. In hot corinos and low-mass protostellar objects, H_2CO transitions have been useful to estimate physical and chemical conditions (Maret et al. 2004; Sahu et al. 2018;

Martín-Doménech et al. 2019). In the Horsehead photodissociation region (PDR), Guzmán et al. (2013) analyzed observations of H_2CO and CH_3OH to investigate their chemistry and dominant formation routes. In massive star-forming regions, H_2CO transitions have been observed in hot molecular cores. In addition, an H_2CO maser at 6 cm has been proposed as an exclusive tracer of high-mass star formation (Pratap et al. 1994; Araya et al. 2015). In the IRAS 16562–3959 high-mass star-forming region, Taniguchi et al. (2020) observed H_2CO and investigated its formation pathways; they also analyzed the emission of $(CH_3)_2CO$ and CH_3OCHO. The identification of both simple and complex organic molecules contributes to our understanding of the chemical network of reactions that interplay these species under interstellar conditions (e.g., Horn et al. 2004; Singh et al. 2022). In evolved stellar objects, Ford et al. (2004) observed H_2CO toward the carbon star IRC +10216 and discussed the H_2CO formation in the context of solar system comet comae. In sources outside the Milky Way, Tang et al. (2021) observed H_2CO to construct a map of the kinetic temperature of two massive star-forming regions in the Large Magellanic Cloud (LMC). Shimonishi et al. (2016) analyzed observations of H_2CO, among other chemical species, to diagnose and claim the first detection of a hot molecular core in the LMC.

The physical conditions of the formaldehyde isotopologues are also investigated here. In a study about deuterated molecules in Orion KL, Neill et al. (2013) estimated D/H
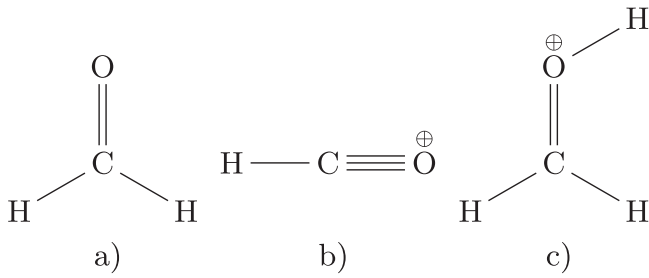
Figure 1. Representation of the neutral molecule (a) formaldehyde and the molecular ions (b) formyl cation and (c) protonated formaldehyde.

ratios from formaldehyde and other molecules using data from Herschel/HIFI. As a rare isotopic species, Turner (1990) detected D_2CO via four transitions toward Orion KL. Nonetheless, Neill et al. (2013) did not confirm such a detection. In a sample of Galactic molecular sources, Yan et al. (2019) performed a study of the $^{12}C/^{13}C$ ratio using transitions from the $H_2^{12}CO$ and $H_2^{13}CO$ isotopologues. With respect to $H_2C^{18}O$, a few works have reported its detection. Using ALMA observations, Persson et al. (2018) detected not only $H_2C^{18}O$ but also $H_2C^{17}O$, $D_2^{13}CO$, and $HDC^{18}O$ toward IRAS 16293–2422 B.

In chemical association with H_2CO, we also present results for the molecular ions HCO^+ and H_2COH^+ (Figure 1). The HCO^+ and its isotopologues have been observed in hot molecular cores and outflows (Sánchez-Monge et al. 2013; Shimonishi et al. 2016). In previous works, Merello et al. (2013) and Hervías-Caimapo et al. (2019) reported preliminary results for $H^{13}CO^+$ in G331.512–0.103 (hereafter G331). Detection of the rare molecular ion H_2COH^+ has scarcely been reported in the literature. It has been observed toward Sgr B2, Orion KL, W51, and the prestellar core L1689B (Ohishi et al. 1996; Bacmann et al. 2016).

The chemical species H_2CO, HCO^+, and H_2COH^+ participate and compete in various chemical reactions, for instance,

$$H_2CO + HCO^+ \longrightarrow H_2COH^+ + CO. \qquad (1)$$

The kinetic constants were experimentally studied in an early work by Tanner et al. (1979). Bacmann et al. (2016) observed H_2COH^+ in the prestellar source L1689B and discussed the reaction presented in Equation (1) in the context of cold prestellar cores. The three species studied here, H_2CO, HCO^+, and H_2COH^+, also play a key role in the gas–grain chemistry to form complex organic molecules, such as glycolaldehyde and sugar-related molecules (Halfen et al. 2006; Woods et al. 2012; Eckhardt et al. 2018; Layssac et al. 2020). Additionally, it is worth mentioning that H_2CO is closely associated with methanol (CH_3OH), a pivotal molecule for interstellar chemical complexity. Studies have demonstrated that successive hydrogenation reactions of carbon monoxide (CO) can lead to the formation of both H_2CO and CH_3OH (Watanabe et al. 2003; Tsuge et al. 2020).

The present work is based on observations of G331, a massive protostellar object embedded in the G331.5–0.1 giant molecular cloud (GMC). The central object drives a powerful outflow with a flow mass and momentum of $\sim 55\,M_\odot$ and $\sim 2.4 \times 10^3\,M_\odot$ km s^{-1}, respectively (Bronfman et al. 2008). The source is located in the tangent region of the Norma spiral arm at a heliocentric distance of ~ 7.5 kpc. Regarding the ambient core of G331, ALMA observations provide evidence

of a lukewarm gas with $n_{H_2} \sim 5 \times 10^6$ cm^{-3} and $T \sim 70$ K (Hervías-Caimapo et al. 2019). In association with those gas conditions, Canelo et al. (2021) and Santos et al. (2022) reported results for the physical and chemical conditions of isocyanic acid (HNCO) and methyl acetylene (CH_3CCH). Here we contribute with new results about the lukewarm and cold gas conditions of G331, which are based on a broad spectral survey collected with the Atacama Pathfinder Experiment (APEX).

In massive protostellar objects, the chemical scenario of the formation of hydrocarbons and carbon chain and organic compounds is not yet well understood (Taniguchi et al. 2018; Kalvāns 2021). In view of the importance of understanding how gas–grain processes occur in massive protostellar objects, this work also presents a chemical model for understanding the cold chemistry that connects two abundant species, such as H_2CO and HCO^+, with a low abundant ion, such as H_2COH^+. In addition, this study allowed us to venture the age of the protostellar object G331. This paper is organized as follows. Section 2 describes the observations carried out by APEX of the source G331 and the methodology used for this study. Section 3 presents the results of the spectral analysis and the estimated physical conditions of G331. In Section 4, the astrophysical and astrochemical implications of the present results are discussed. Final remarks and conclusions are summarized in Section 5. Additionally, an Appendix has been included to provide supplementary information and data.

2. Methodology

The APEX telescope (Güsten et al. 2006) was used to perform the observations, adopting the single point mode, toward the source coordinates R.A., decl. $= 16^h 12^m 10\overset{s}{.}1$, $-51°28'38\overset{''}{.}1$. The APEX-1 and APEX-2 receivers of the Swedish Heterodyne Facility Instrument (Vassilev et al. 2008) were used to collect spectral setups in the frequency ranges of 213–275 and 267–378 GHz, respectively. The spectral resolution of the data set was adjusted to be between ~ 0.15 and 0.25 km s^{-1} for a noise level of about 30 mK across the bands.

As part of the observational runs, the SEPIA B5 instrument (Belitsky et al. 2018) was used to collect setups between 159 and 211 GHz. SEPIA B5 is a dual-polarization sideband-separated receiver. The lower and upper sidebands are separated by 12 GHz. Each sideband is recorded by two XFFTS units of 2.5 GHz with a 1 GHz overlap. The half-power beamwidth values covered by the APEX receivers range from $\sim 17''$ to $39''$ and are estimated for each transition using $7\overset{''}{.}8 \times 800/\nu$[GHz] (Güsten et al. 2006; Quénard et al. 2017),[5] where ν is the rest frequency of the spectra. With respect to the calibration uncertainty, Dumke Mac-Auliffe (2010) discussed how lines of $C^{18}O$ (3–2) and ^{13}CO (3–2) might reach uncertainties of $\sim 13\%$ and lines of H_2CO and CH_3OH of up to $\sim 33\%$. Considering that we observed different species through a multiwavelength analysis, an overall calibration uncertainty of 30% was adopted.

The data reduction was carried out with the CLASS package of GILDAS.[6] The spectra obtained from the APEX real-time calibration tool (Muders et al. 2006) in the CLASS data architecture are in the corrected antenna temperature scale.[7] For

---

[5] https://www.apex-telescope.org/ns/instruments/
[6] https://www.iram.fr/IRAMFR/GILDAS/
[7] https://www.apex-telescope.org/telescope/efficiency/

further clarity, we exhibit spectra in units of antenna temperature (K) with respect to the systemic velocity of G331 ($V_{lsr} = -90$ km s^{-1}). Additionally, all of the spectra were smoothed to exhibit a common channel of 1 km s^{-1}. The Weeds[8] extension of CLASS (Maret et al. 2011), along with the spectroscopic databases Cologne Database for Molecular Spectroscopy (CDMS[9]; Endres et al. 2016) and JPL[10] (Pickett et al. 1998), were also used here. The CASSIS[11] software was used to estimate the physical conditions from the spectral lines, which were utilized in the main-beam temperature (T_{mb}) scale adopting the main-beam efficiencies $\eta_{mb} = 0.80, 0.75$, and 0.73 for SEPIA180, APEX-1, and APEX-2, respectively. In order to evaluate the beam dilution effects, a source size of 5″ was adopted for the G331 core and 15″ for an expanded region. Using the CASSIS tools, local thermodynamic equilibrium (LTE) analyses were performed using calculations and the population diagram method (Goldsmith & Langer 1999; Mangum & Shirley 2015; Roueff et al. 2021). Non-LTE calculations were carried out with the RADEX code (van der Tak et al. 2007) using rate coefficients from the LAMDA database.[12]

2.1. Chemical Models

The gas–grain code NAUTILUS was used to compute abundances as a function of time from a network of gas and grain chemical reactions (Semenov et al. 2010; Reboussin et al. 2014; Ruaud et al. 2015, 2016). We focused on computing the abundances of H_2CO, HCO^+, and H_2COH^+ considering similar conditions to those obtained from the observations. NAUTILUS uses the KIDA[13] database (Wakelam et al. 2015), which includes rate coefficients for a total of about 7509 reactions and 489 chemical species. For the solid-state chemistry, it considers the mantle and surface mechanisms investigated by Hasegawa & Herbst (1993) and Ghesquière et al. (2015). For the neutral and molecular ions analyzed in this work, there is a network of no more than 50 chemical reactions connecting them. The chemistry of HCO^+ and H_2CO is significant, and the detection of various of their isotopologues suggests gas–grain processes in cold environments. Previous studies unveiled a rich chemistry in the lukewarm regions of G331 ($T_g \approx 70$ K) evidenced from various spectral lines of HNCO and CH_3CCH (Canelo et al. 2021; Santos et al. 2022). Here we expand the chemical models of G331 adopting a cold gas condition ($T_g \approx 50$ K), which might explain not only the abundances of H_2CO, HCO^+, and H_2COH^+ but also the eventual formation of more complex molecules.

3. Results

3.1. Line Analysis

3.1.1. Formaldehyde and Its Isotopologues

The isotopologues $H_2^{12}CO$, $H_2^{13}CO$, HDCO, and $H_2C^{18}O$ were identified in a frequency interval of $\sim$190–357 GHz through 35 transition lines whose assignments, specifying the ortho or para

character of the states for the symmetric isotopologues (e.g., Clouthier & Ramsay 1983; Chapovsky 2001), spectroscopic data, and Gaussian fit parameters, are given in Table 1. The spectral analysis was primarily performed on lines with significantly stronger signals than the limit of detection (3σ level) that are exhibited in the different panels of Figure 2. In agreement with the expected isotopic abundances, the most and least abundant isotopologues, $H_2^{12}CO$ and $H_2C^{18}O$, respectively, exhibited the strongest and weakest line intensities, respectively. Despite $H_2C^{18}O$ being a rare isotopologue (e.g., Müller & Lewen 2017), we could detect it via five spectral lines.

The main isotopologue, (o, p)-H_2CO, was detected via nine lines, although the lines at $\sim$291,380.48 and 291,384.26 MHz, corresponding to the transitions $4_{3,2}-3_{3,1}$ and $4_{3,1}-3_{3,0}$, respectively, can be considered partially resolved (see Figure 2(a)). Various H_2CO transitions detected in this work were also reported in sources such as OMC-1 and Orion KL and in high-mass star-forming regions (e.g., Loren 1984; Wootten et al. 1984; Mangum et al. 1990; Taniguchi et al. 2020).

Thirteen spectral lines of (o, p)-$H_2^{13}CO$ were identified, although two of them, at the rest frequencies $\sim$284,117.45 and 284,120.62 MHz, were deemed partially resolved (see Figure 2(b)). As expected, the intensities of the $H_2^{13}CO$ lines are lower than those of H_2CO. By comparing the integrated areas of neighboring lines, e.g., o-$H_2^{13}CO$ at $\sim$219,908.52 MHz and o-H_2CO at $\sim$225,697.77 MHz, the $H_2CO/H_2^{13}CO$ ratio is about 16. In previous works, Jewell et al. (1989) and Helmich & van Dishoeck (1997) observed various of the $H_2^{13}CO$ transitions in G331.

The HDCO isotopologue was detected via eight spectral lines (see Figure 2(c)). It can be noted that the HDCO line profiles exhibit a partial asymmetry with a blueshifted emission wing. In an investigation of HNCO in G331, Canelo et al. (2021) not only observed similar spectral asymmetries but also found them to be more pronounced in some specific K-ladder transitions of HNCO. These findings were discussed in the context of molecular outflows (e.g., Canelo et al. 2021 and references therein). In this work, we expect that the HDCO emission may be linked to an expanded gas region influenced by the molecular outflow. However, to better understand the emission of spectral tracers potentially associated with the molecular outflow, it is crucial to conduct further investigations, including the development of models that consider the core and outflow of G331.

In addition, five spectral lines of the (o, p)-$H_2C^{18}O$ isotopologue were clearly identified and are shown in Figure 2(d). From this study toward G331, we confirm the observation of the transitions of the rare isotopologue $H_2C^{18}O$ previously reported toward other sources (e.g., Mangum et al. 1990; Sutton et al. 1995).

The successful detection of HDCO prompted further investigation into the presence of doubly deuterated formaldehyde (D_2CO), which has been scarcely observed in objects of the ISM (e.g., Turner 1990; Ceccarelli et al. 1998). As a result, we report the tentative detection of p-D_2CO $3_{1,3}-2_{1,2}$ at a rest frequency of $\sim$166,102.74 MHz previously detected in prestellar cores (Bacmann et al. 2003). Figure 3(a) shows this spectral line whose emission is above the limit of detection but shifted from the source systemic velocity ($V_{lsr} = -90$ km s^{-1}). This makes us think that a possible candidate for this line might

Table 1
Spectral Line Analysis of $H_2^{12}CO$, $H_2^{13}CO$, HDCO, and $H_2C^{18}O$

Species and Transitions	Frequency[a] (MHz)	Beamwidth (arcsec)	E_u (K)	g_u	A_{ul} (10^{-5} s^{-1})	Line Area (K km s^{-1})	V_{lsr} (km s^{-1})	Line Width (km s^{-1})	rms (mK)
p-H$_2$CO (3 0 3–2 0 2)	218,222.192	28.56	20.96	7	28.2	12.99 ± 0.07	−90.07 ± 0.02	6.4 ± 0.04	47
p-H$_2$CO (3 2 2–2 2 1)	218,475.632	28.56	68.09	7	15.7	5.5 ± 0.3	−90.4 ± 0.1	5.9 ± 0.3	35
p-H$_2$CO (3 2 1–2 2 0)	218,760.066	28.52	68.11	7	15.8	5.04 ± 0.04	−90.33 ± 0.02	5.85 ± 0.05	36
o-H$_2$CO (3 1 2–2 1 1)	225,697.775	27.65	33.45	21	27.7	17.88 ± 0.06	−90.2 ± 0.01	7.25 ± 0.03	38
p-H$_2$CO (4 0 4–3 0 3)	290,623.405	21.47	34.9	9	69	16.1 ± 0.1	−90.39 ± 0.03	7.29 ± 0.08	42
p-H$_2$CO (4 2 3–3 2 2)	291,237.78	21.43	82.07	9	52.1	10.92 ± 0.03	−90.578 ± 0.009	7.13 ± 0.02	33
o-H$_2$CO (4 3 2–3 3 1)	291,380.488	21.41	140.94	27	30.4	9.653 ± 1E-3	−90.36 ± 0.02	6.73 ± 0.04	28
o-H$_2$CO (4 3 1–3 3 0)	291,384.264	21.41	140.94	27	30.4	12 ± 0.1	−90.38 ± 0.04	7.75 ± 0.09	29
o-H$_2$CO (5 1 5–4 1 4)	351,768.645	17.74	62.45	33	120	14.7 ± 0.2	−90.88 ± 0.04	7.1 ± 0.1	46
o-H$_2^{13}$CO (3 1 3–2 1 2)	206,131.626	30.27	31.62	21	21.1	1.68 ± 0.02	−90.91 ± 0.03	4.37 ± 0.08	18
o-H$_2^{13}$CO (3 1 2–2 1 1)	219,908.525	28.37	32.94	21	25.6	1.14 ± 0.04	−91.01 ± 0.06	3.6 ± 0.2	34
o-H$_2^{13}$CO (4 1 4–3 1 3)	274,762.112	22.71	44.8	27	54.7	2.49 ± 0.04	−90.94 ± 0.03	4.47 ± 0.08	32
o-H$_2^{13}$CO (4 3 2–3 3 1)	284,117.45	21.96	140.47	27	28.2	1.55 ± 0.05	−92.1 ± 0.1	7.3 ± 0.3	21
o-H$_2^{13}$CO (4 3 1–3 3 0)	284,120.62	21.96	140.47	27	28.2	1.1 ± 0.1	−90.5 ± 0.4	6.3 ± 0.7	18
p-H$_2^{13}$CO (4 2 2–3 2 1)	284,632.42	21.92	81.43	9	48.6	0.59 ± 0.02	−91.54 ± 0.05	3.4 ± 0.1	17
o-H$_2^{13}$CO (4 1 3–3 1 2)	293,126.515	21.29	47.01	27	66.4	2.25 ± 0.08	−91.2 ± 0.07	4.2 ± 0.2	42
o-H$_2^{13}$CO (5 1 5–4 1 4)	343,325.713	18.17	61.28	33	112	2.45 ± 0.09	−90.93 ± 0.07	4.3 ± 0.2	30
p-H$_2^{13}$CO (5 0 5–4 0 4)	353,811.872	17.64	51.02	11	127	1.54 ± 0.04	−91.22 ± 0.05	3.8 ± 0.1	33
p-H$_2^{13}$CO (5 2 4–4 2 3)	354,898.595	17.58	98.41	11	108	0.83 ± 0.05	−91.3 ± 0.1	4.0 ± 0.3	34
o-H$_2^{13}$CO (5 3 3–4 3 2)	355,190.9	17.57	157.52	33	82.5	1.39 ± 0.04	−90.81 ± 0.08	5.9 ± 0.2	29
o-H$_2^{13}$CO (5 3 2–4 3 1)	355,202.601	17.57	157.52	33	82.5	1.21 ± 0.03	−90.79 ± 0.07	5.1 ± 0.2	32
p-H$_2^{13}$CO (5 2 3–4 2 2)	356,176.243	17.52	98.52	11	109	1.02 ± 0.03	−91.04 ± 0.08	5.2 ± 0.2	32
HDCO (3 0 3–2 0 2)	192,893.27	32.35	18.53	7	19.4	1.03 ± 0.02	−90.73 ± 0.06	5.2 ± 0.1	21
HDCO (3 1 2–2 1 1)	201,341.35	30.99	27.29	7	19.6	0.956 ± 0.008	−91.02 ± 0.02	5.25 ± 0.05	18
HDCO (4 1 4–3 1 3)	246,924.6	25.27	37.6	9	39.6	1.06 ± 0.04	−90.73 ± 0.09	4.3 ± 0.2	47
HDCO (4 0 4–3 0 3)	256,585.43	24.32	30.85	9	47.4	1.25 ± 0.05	−91.11 ± 0.08	4.6 ± 0.2	50
HDCO (4 1 3–3 1 2)	268,292.02	23.26	40.17	9	50.8	0.85 ± 0.03	−91.06 ± 0.09	4.1 ± 0.2	37
HDCO (5 1 5–4 1 4)	308,418.2	20.23	52.4	11	80.8	1.54 ± 0.02	−91.14 ± 0.02	4.72 ± 0.07	20
HDCO (5 0 5–4 0 4)	319,769.68	19.51	46.19	11	93.7	1.41 ± 0.03	−91.31 ± 0.05	4.5 ± 0.1	37
HDCO (5 1 4–4 1 3)	335,096.739	18.62	56.25	11	104	1.43 ± 0.02	−91.04 ± 0.04	4.76 ± 0.09	28
o-H$_2$C^{18}O (3 1 3–2 1 2)	201,614.256	30.95	31.22	21	19.7	0.473 ± 0.009	−90.83 ± 0.05	4.8 ± 0.1	18
p-H$_2$C^{18}O (3 0 3–2 0 2)	208,006.441	29.99	19.97	7	24.4	0.134 ± 0.007	−91.17 ± 0.09	3.4 ± 0.2	17
o-H$_2$C^{18}O (4 1 4–3 1 3)	268,745.789	23.22	44.12	27	51.1	0.76 ± 0.04	−90.7 ± 0.1	4.9 ± 0.3	48
o-H$_2$C^{18}O (4 1 3–3 1 2)	286,293.96	21.79	46.23	27	61.8	0.64 ± 0.02	−91.01 ± 0.06	4.3 ± 0.2	23
o-H$_2$C^{18}O (5 1 5–4 1 4)	335,816.025	18.58	60.24	33	105	0.85 ± 0.02	−90.99 ± 0.06	4.8 ± 0.1	24

Note.
[a] Rest frequency values, obtained from databases such as CDMS (Endres et al. 2016) and JPL (Pickett et al. 1998), are accessed using the CASSIS software (Vastel et al. 2015; see Section 2 for more details). The last column indicates the rms noise of the spectra.

also be OC^{34}S (14–13) at 166,105.75 MHz. A second tentative identification is displayed in Figure 3(b). The o-D$_2$CO $5_{0,5}$–$4_{0,4}$ transition was also tentatively identified, but a dominant line, likely blended with SO$_2$ $v = 0$ at ~287,485.44 MHz, avoided a clear identification.

3.1.2. The Formyl Cation and Its Isotopologues

The isotopologues of the formyl cation (HCO$^+$, H^{13}CO$^+$, DCO$^+$, HC^{18}O$^+$, and HC^{17}O$^+$) were also sought in G331. Eight lines from these isotopologues were identified, except the deuterated DCO$^+$, of which the spectroscopic and fitted parameters are given in Table 2. The two rotational lines of the main isotopologue HCO$^+$ and their fits are shown in Figure 4. The HCO$^+$ spectra exhibited broad spectral wings, from −150 to −30 km s^{-1}, and they were better described by Lorentzian than Gaussian functions. The Lorentzian profile suggests that the HCO$^+$ emission is likely affected by the molecular outflow (Hervías-Caimapo et al. 2019).

The spectral lines of H^{13}CO$^+$, HC^{18}O$^+$, and HC^{17}O$^+$ did not exhibit Lorentzian profiles with broad wings. Thus, Gaussian functions, instead of Lorentzian ones, were used to fit the spectra. The spectra of these isotopologues are exhibited in the different panels of Figure 5. For all of the identified HCO$^+$ isotopologues, the $J = 2$–1 transition was observed. Considering the velocity-integrated temperatures for the line profiles of this transition, the ratios HCO$^+$:H^{13}CO$^+$:HC^{18}O$^+$:HC^{17}O$^+$ ≈ 64:21:3:1 were obtained. Nevertheless, the results based on LTE and non-LTE methods will be given in the next section.

It is worth highlighting that the deuterated formyl cation DCO$^+$ was not detected in spite of the isotopologue HDCO being identified through several lines. In contrast, the ^{17}O isotopologue of the formyl cation was detected but not the isotopologue of formaldehyde H$_2$C^{17}O. Those aspects demand follow-up studies due to their implications for the understanding of the isotopic fraction and the evolution of protostellar objects.
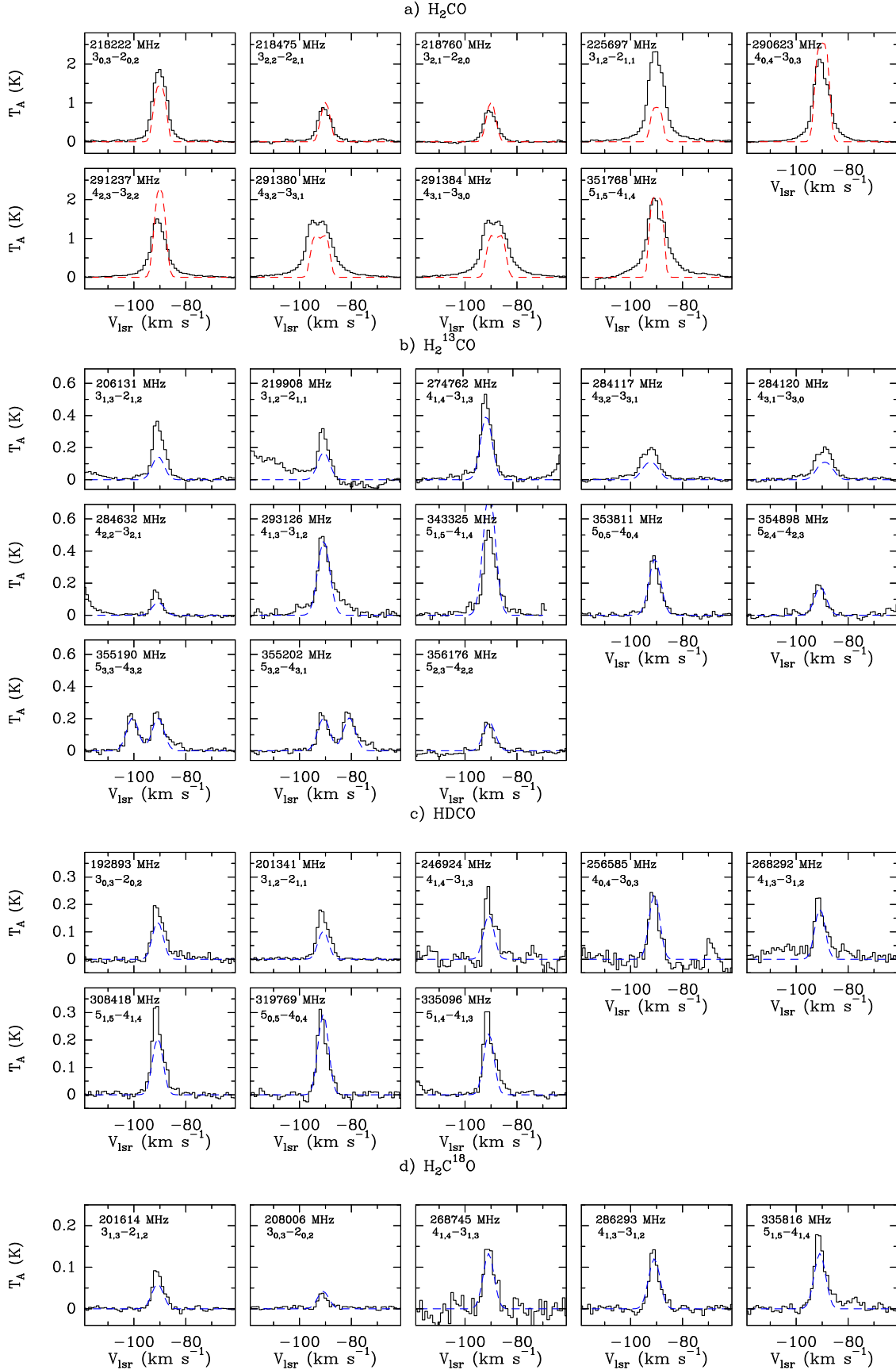
Figure 2. Observed (solid) and modeled (dashed) spectra from the LTE (blue) and non-LTE (red) simulations (Section 3.2) of the formaldehyde isotopologues in G331: (a) H_2CO, (b) $H_2^{13}CO$, (c) HDCO, and (d) $H_2C^{18}O$. For each spectrum, the y-axis represents the intensity on a scale of antenna temperature (K), while the x-axis represents the velocity relative to the local standard of rest (systemic $V_{lsr} = -90$ km s^{-1}).
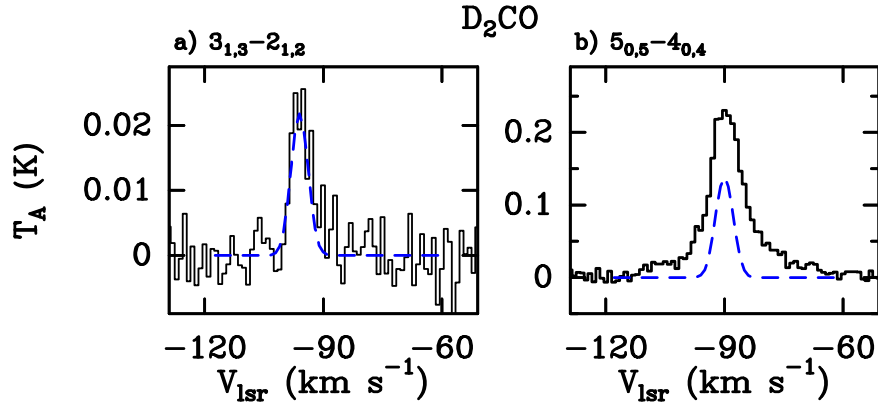
Figure 3. Tentative identification of D_2CO: (a) p-D_2CO $3_{1,3}$–$2_{1,2}$ at a frequency of ~166,102.74 MHz and appearing at $V_{lsr} \approx -96$ km s^{-1} and (b) o-D_2CO $5_{0,5}$–$4_{0,4}$ at a frequency of ~287,485.65 MHz but likely dominated by emission of SO_2 at 287,485.44 MHz. Under the upper limit condition $N(D_2CO) < N(HDCO)$ and FWHM = 5 km s^{-1}, the dashed lines indicate hypothetical LTE models of D_2CO.

Table 2
Spectral Line Analysis of the Molecular Ions HCO^+, $H^{13}CO^+$, $HC^{18}O^+$, $HC^{17}O^+$, and H_2COH^+

Species and Transitions	Frequency (MHz)	Beamwidth (arcsec)	E_u (K)	A_{ul} (10^{-5} s^{-1})	Line Area (K km s^{-1})	V_{lsr} (km s^{-1})	Line Width (km s^{-1})	rms (mK)
HCO^+ (2–1)[a]	178,375.056	34.98	12.84	40.2	20 ± 2	-91.56 ± 0.02	6.97 ± 0.07	120
HCO^+ (3–2)[a]	267,557.626	23.32	25.68	145	31 ± 3	-91.21 ± 0.03	9.2 ± 0.1	133
$H^{13}CO^+$ (2–1)	173,506.700	35.96	12.49	37	6.41 ± 0.02	-89.631 ± 0.006	4.93 ± 0.01	13
$H^{13}CO^+$ (3–2)	260,255.339	23.97	24.98	134	7.05 ± 0.05	-89.94 ± 0.02	5.14 ± 0.04	53
$H^{13}CO^+$ (4–3)	346,998.344	17.98	41.63	329	6.25 ± 0.02	-90.205 ± 0.007	5.19 ± 0.02	22
$HC^{18}O^+$ (2–1)	170,322.626	36.63	12.26	35	1.05 ± 0.01	-89.69 ± 0.03	4.37 ± 0.07	11
$HC^{18}O^+$ (3–2)	255,479.389	24.42	24.52	127	1.14 ± 0.04	-89.86 ± 0.08	4.5 ± 0.2	44
$HC^{17}O^+$ (2–1)	174,113.169	35.83	12.53	37.4	0.31 ± 0.01	-89.5 ± 0.1	5.1 ± 0.3	11
H_2COH^+ (3 0 3–2 0 2)	190,079.131	32.82	18.26	6.59	0.16 ± 0.01	-89.9 ± 0.2	4.5 ± 0.5	12
H_2COH^+ (5 1 4–5 0 5)	207,964.754	30.00	55.51	14.7	0.12 ± 0.01	-91.6 ± 0.2	5.6 ± 0.8	17
H_2COH^+ (4 0 4–3 0 3)	252,870.339	24.67	30.39	16.1	0.23 ± 0.05	-90.7 ± 0.3	3.2 ± 0.9	44
H_2COH^+ (10 1 9–10 0 10)[b]	348,102.330	17.92	181.67	48.2	0.4 ± 0.1	-91.6 ± 0.4	7 ± 2	30

Notes.
[a] The line fit parameters of the HCO^+ lines were obtained using Lorentzian functions. The last column indicates the rms noise of the spectra.
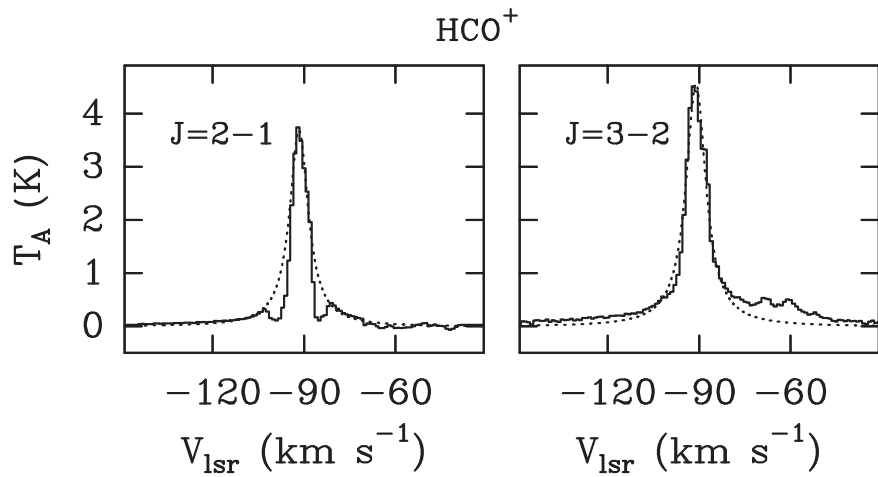[b] Line likely blended with $^{34}SO_2$.

Figure 4. Spectral lines (solid lines) and Lorentzian fits (dotted lines) of the transitions 2–1 and 3–2 of HCO^+ identified at the rest frequencies ~178,375.05 and 267,557.62 MHz, respectively.
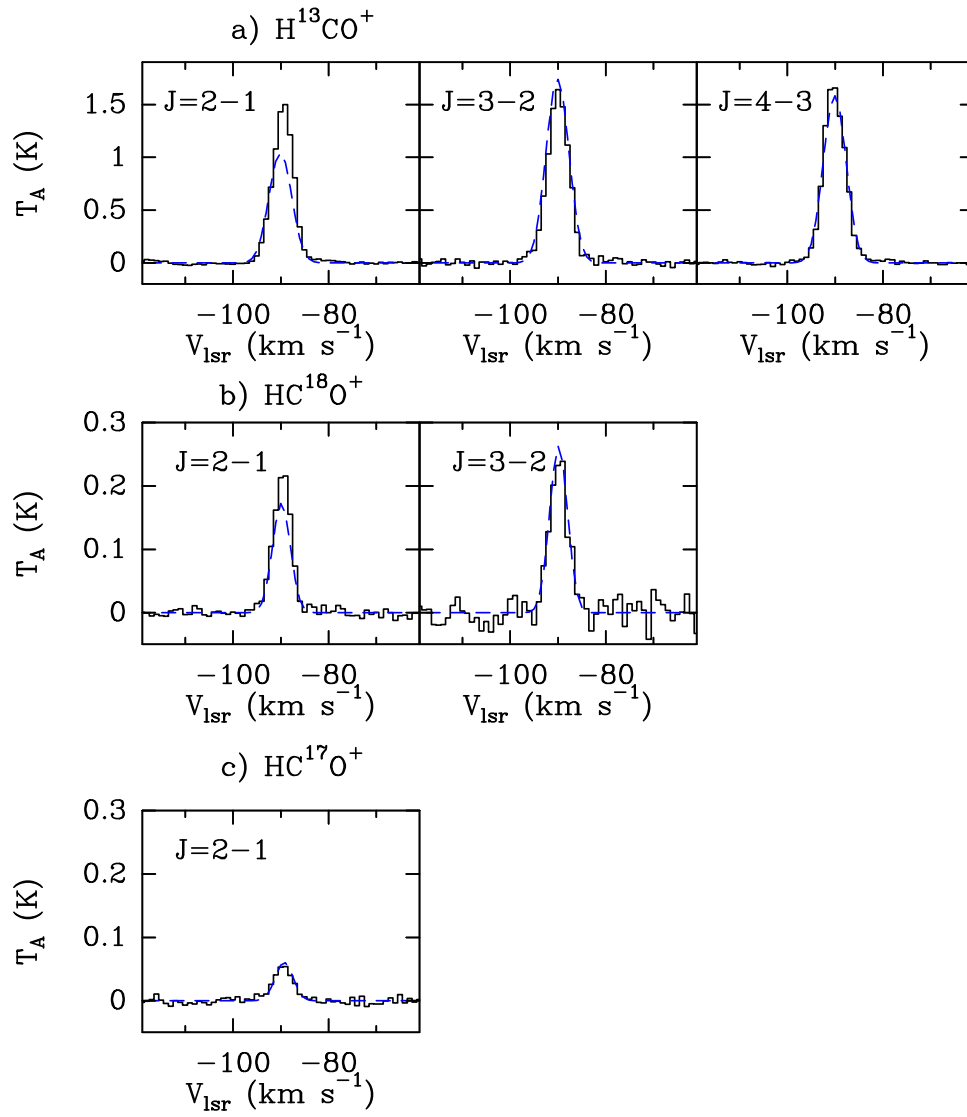
Figure 5. Similar to Figure 2 but for the isotopologues of the formyl cation with their LTE models: (a) $H^{13}CO^+$, (b) $HC^{18}O^+$, and (c) $HC^{17}O^+$.
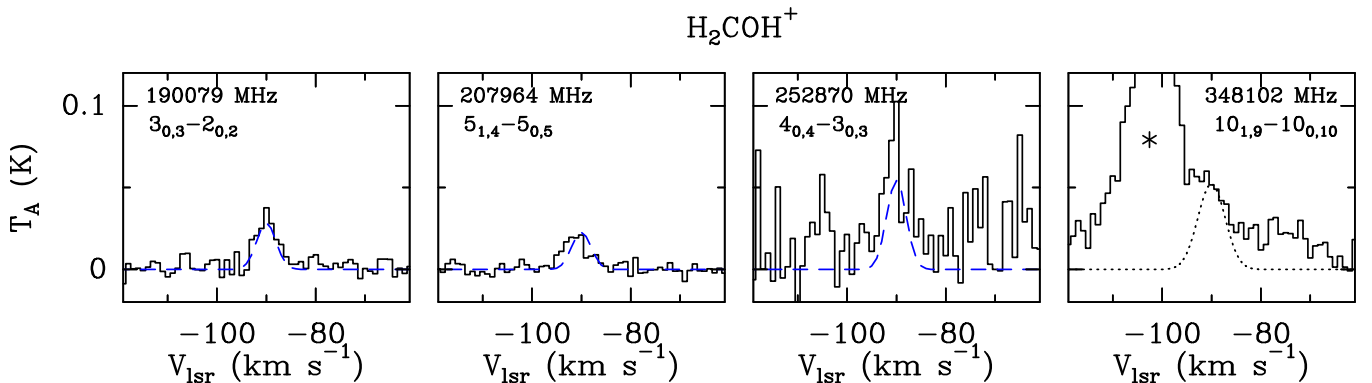

Figure 6. Similar to Figure 2 but for the spectral lines of H_2COH^+ with their LTE models (dashed lines). In the fourth panel, the Gaussian fit depicts an H_2COH^+ transition tentatively identified at $\sim348,102.330$ MHz. The asterisk indicates a line likely blended with $^{34}SO_2$ at $\sim348,117$ MHz.

3.1.3. Protonated Formaldehyde

The search for H_2COH^+ was performed across a frequency range of ~159–356 GHz. As a result, the identified lines of H_2COH^+ are exhibited in Figure 6 and were adjusted by means of Gaussian functions. The spectroscopic and fit parameters are listed in Table 2. In Figure 6, the first three spectra are identified without blended emission at a rest frequencies of $\sim190,079.13$, 207,964.75, and 252,870.34 MHz; in the fourth panel, a tentative identification was made at $\sim348,102.33$ MHz. The detection is unclear due to a spectral signature that dominates the whole spectrum; it is likely associated with $^{34}SO_2$ at $\sim348,117$ MHz (e.g., Jewell et al. 1989).

In this work, the detection of H_2COH^+ is reported for the first time in a hot molecular core such as G331. This cation was identified by Ohishi et al. (1996) across a frequency range of $\sim$31–174 GHz toward massive star-forming regions but not in cold and dark clouds. Bacmann et al. (2016) detected H_2COH^+ across a frequency range of $\sim$102–168 GHz in a cold ($\sim$10 K) source, the prestellar core L1689B. By means of a different technique of observation, Meier et al. (1993) detected H_2COH^+ in the coma of comet P/Halley with a neutral mass spectrometer on the Giotto spacecraft.

3.2. Physical Conditions

The temperature and column densities of the molecular species were estimated using LTE and non-LTE conditions. The LTE methods were applied to analyze the physical conditions of all of the detected isotopologues of formaldehyde, the formyl cation, and protonated formaldehyde (H_2COH^+). Non-LTE hypotheses were considered to infer the physical conditions of the ^{12}C isotopologues, H_2CO, and HCO^+. All of the analyses were performed under the general assumption of a source size of $5''$. In the particular case of HCO^+, a second solution adopting $15''$ was tested too.

When the LTE approximation was assumed, the population diagram method was used to estimate the excitation conditions of the molecular species, i.e., the total column densities (N) and excitation temperatures (T_{exc}), by means of

$$\ln \frac{N_u}{g_u} = \ln \frac{N}{Q} - \frac{E_u}{kT_{exc}}, \quad (2)$$

where N_u, g_u, E_u, and Q are the column density, the degeneracy of the upper state, the energy of the upper level involved in the transition, and the partition function, respectively. In Table 1, the upper state degeneracy $g_u = (2J_u + 1)g_{ns}^{(u)}$ was given for each detected transition, where J_u and $g_{ns}^{(u)}$ are the rotational angular momentum and the nuclear spin statistical weight of the upper state (Bunker & Jensen 1989). The optical depth (τ) has been inferred using the population diagram method. For a given transition, this can be estimated using the expression

$$\tau = \frac{c^3 A_{ul} N_u}{8\pi\nu^3 \Delta v \sqrt{\pi}/2\sqrt{\ln 2}} [\exp(h\nu/kT_{exc}) - 1], \quad (3)$$

where Δv and A_{ul} represent the spectral line width (km s^{-1}) and the Einstein coefficients (s^{-1}), respectively (Goldsmith & Langer 1999; Mangum & Shirley 2015; Vastel et al. 2015).

3.2.1. Formaldehyde Isotopologues: LTE Analyses

The population diagrams of the ^{13}C, D, and ^{18}O isotopologues of formaldehyde have been obtained with updated values of the partition function (see the Appendix), and Equation (2) can be corrected by taking into account the optical depth (τ) applied when the gas emission tends to be optically thick and the beam dilution factors, which allow us to constrain the size of the emitting region with respect to the antenna beam (Goldsmith & Langer 1999). The population diagrams of $H_2^{13}CO$, HDCO, and $H_2C^{18}O$ are exhibited in Figure 7 (panels (a), (b), and (c), respectively) and were obtained after applying a beam dilution correction for an emitting source assumed to be $5''$ and observed with an antenna beam ranging from $\sim$17$''$ to 39$''$.

$H_2^{13}CO$. This population diagram was plotted using the 13 detected lines corresponding to transitions in the $E_u \approx 31$–158 K range (Figure 7(a)). The linear fit provided the result $T_{exc} = 82.9 \pm 21.8$ K and $N = (8.0 \pm 2.0) \times 10^{14}$ cm^{-2} ($\chi^2_{red} = 1.53$). From this result, synthetic spectra were computed and compared with the observed lines in Figure 2. The values of the optical depth were estimated to be $\tau \lesssim 1$ for all spectra except for the partially blended lines at $\sim$284,117.45 and 284,120.62 MHz, in agreement with the LTE formalism.

In comparison with previous works, Schöier et al. (2002) carried out radiative analyses of $H_2^{13}CO$ based on transitions in the $E_u \approx 21$–99 K range toward the low-mass protostellar object IRAS 16293$-$2422. They reported an excitation temperature of around 90 K.

$HDCO$. Based on its eight spectral lines, detected in the range $E_u \approx 18$–56 K, the population diagram is displayed in Figure 7(b). From the linear fit, $T_{exc} = 20.8 \pm 3.5$ K and $N = (2.5 \pm 0.8) \times 10^{14}$ cm^{-2} ($\chi^2_{red} = 0.84$) were obtained. The observed spectral lines and the simulated ones obtained from this result are exhibited in Figure 2, and the values of the optical depth were estimated as $\tau \lesssim 1$.

Neill et al. (2013) performed a study about deuterated molecules in Orion KL. For $H_2^{13}CO$ and HDCO, they discussed different LTE scenarios with temperatures of $\sim$40, 63, and 67 K, as well as particular aspects about the deprotonation of H_2COH^+ and $HDCOH^+$. Bianchi et al. (2017) analyzed several deuterated species toward the class I protostar SVS 13-A. From the population diagrams of $H_2^{13}CO$, HDCO, and D_2CO with source sizes of $\sim$10$''$, they derived temperatures of $\sim$23, 15, and 28 K, respectively.

D_2CO. The LTE calculations were carried out to estimate an upper limit on the D_2CO emission. Taking into account the excitation conditions of HDCO, the D_2CO column density was computed assuming that $N(D_2CO) < N(HDCO) \approx 2.5 \times 10^{14}$ cm^{-2} and $T_{exc} \approx 21$ K. The best solution gave $N(D_2CO) \approx 1.3 \times 10^{14}$ cm^{-2} ($\chi^2_{red} = 0.8$), providing a column density ratio of $D_2CO/HDCO \approx 0.5$.

The D_2CO has been observed in only a few sources. In Orion KL, Neill et al. (2013) established an upper limit on the D_2CO abundance of $[D_2CO]/[HDCO] \leqslant 0.1$. Turner (1990) detected three transitions of D_2CO in Orion KL, reporting $[D_2CO]/[HDCO] = 0.02$. In IRAS 16293$-$2422, a source with several studies of molecular deuteration, Ceccarelli et al. (1998) found $[D_2CO]/[HDCO] \leqslant 0.5$.

$H_2C^{18}O$. The population diagram of this isotopologue was obtained from five detected transition lines that covered the $E_u \approx 19$–60 K range. The linear fit provided $T_{exc} = 30.7 \pm 10.3$ K and $N = (6.8 \pm 3.2) \times 10^{13}$ cm^{-2} ($\chi^2_{red} = 1.23$). From this solution, synthetic spectra were simulated and compared with the observed lines (Figure 2). The spectral lines of $H_2^{18}O$ are optically thin, as expected according to its low abundance. It is worth mentioning that the population diagrams of HDCO and $H_2C^{18}O$ have similar E_u ranges of $\sim$18–60 K, different from those of $H_2^{13}CO$, $E_u \sim 30$–160 K. The excitation temperatures of HDCO and $H_2C^{18}O$ ($T_{exc} \lesssim 30$ K) are lower than the obtained one for $H_2^{13}CO$ ($T_{exc} \approx 83$ K). On the one hand, such a difference might come from the fact that more lines of $H_2^{13}CO$ were observed than HDCO and $H_2C^{18}O$, providing a more extended population diagram. On the other hand, there might be a scenario in which the formaldehyde isotopologues trace different excitation conditions, although to assume this
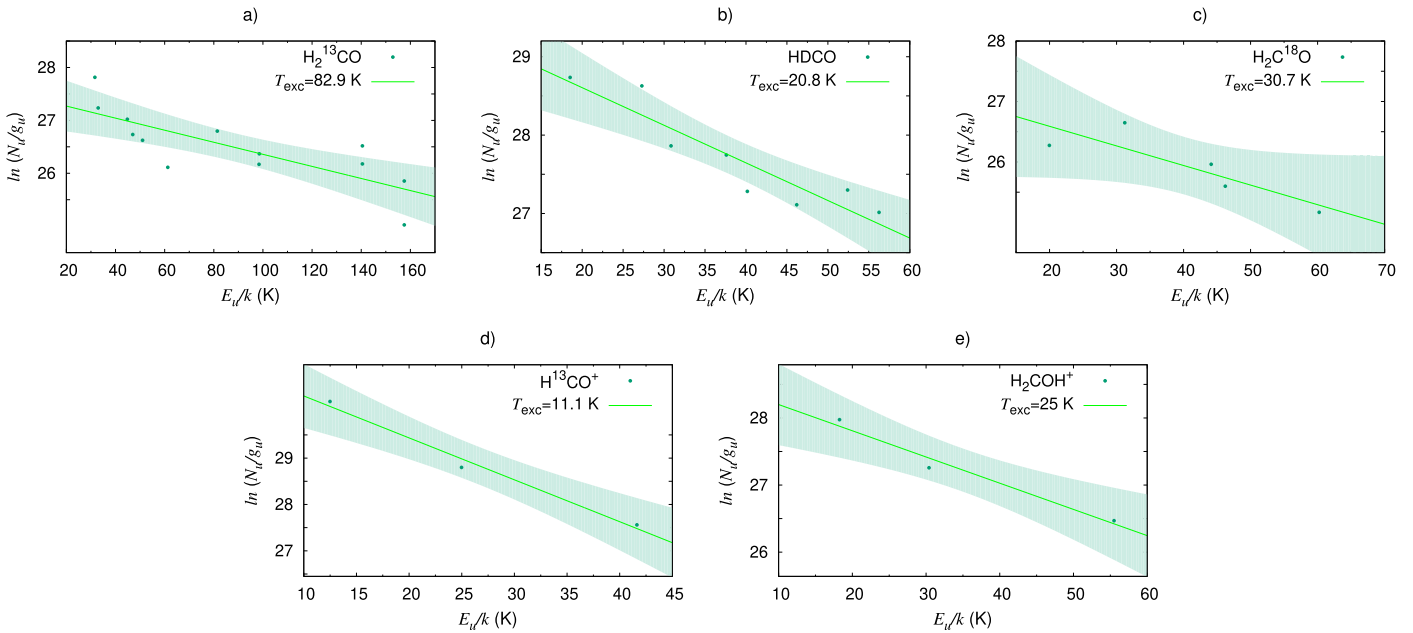
Figure 7. Population diagrams of the formaldehyde isotopologues (a) $H_2^{13}CO$, (b) HDCO, and (c) $H_2C^{18}O$ and the molecular ions (d) $H^{13}CO^+$ and (e) H_2COH^+. The solid line and shaded areas represent the linear regression fits and their (95%) confidence bands for each species.

hypothesis would require further studies including, e.g., gas–grain calculations and chemical models.

3.2.2. H₂CO: Non-LTE Calculations

The physical conditions of H_2CO were calculated using the non-LTE code RADEX, which provides an alternative approach to the population diagram based on the assumption of optically thin emission lines. Within this approach, the optical depth effects are treated with an escape probability method assuming an isothermal and homogeneous medium without large-scale velocity fields (van der Tak et al. 2007). The non-LTE calculations were performed using available excitation rates between o- and p-H_2CO and o- and p-H_2. Wiesenfeld & Faure (2013) reported calculations for the first 81 rotational levels of formaldehyde considering temperatures between $\sim$10 and 300 K. In an earlier work, Troscompt et al. (2009) also discussed the rotational excitation of H_2CO by H_2.

From the five lines of p-H_2CO, the best solution ($\chi^2_{red} = 4.5$) provided $T_{kin} = 87.4 \pm 0.6$ K and $N = (6.2 \pm 0.3) \times 10^{15}$ cm^{-2}. From the four lines of o-H_2CO, $T_{kin} = 95.1 \pm 0.3$ K and $N = (9 \pm 3) \times 10^{15}$ cm^{-2} ($\chi^2_{red} = 3.5$) were obtained. These results provide an ortho-to-para ratio of H_2CO of $\sim$1.4. The H_2 density was also estimated from the calculations $n(H_2) \simeq 4 \times 10^7$ cm^{-3} adopting a source size of 5″. The density of molecular hydrogen was computed using conventional ortho-to-para ratios, whose value can fluctuate between $\sim$0.1 and 3, contingent on the chemistry, physical properties, and evolutionary stage of the sources. In prestellar cores, such a range was discussed from 3 to values even smaller than 0.001 (e.g., Osterbrock 1962; Lacy et al. 1994; Pagani et al. 2013).

Synthetic lines were generated from the non-LTE approximations and compared with the observations in Figure 2(a). Concerning the optical depth of the p-H_2CO transitions, the highest and lowest values were $\sim$4.5 and 0.9 for the lines at $\sim$290,623.40 and 218,760.06 MHz, respectively. Similarly, for the o-H_2CO transitions, the highest and lowest optical depths

were $\sim$5.2 and $\sim$0.7 for the transitions at $\sim$351,768.64 and 291,380 MHz, respectively.

A comparison of our results with other works is useful to show they are in accordance. Schöier et al. (2002) analyzed the physical conditions of H_2CO in IRAS 16293−2422. They estimated temperatures around 90 K and ortho-to-para ratios of H_2CO of around 0.9. Guzmán et al. (2013) used non-LTE models of o- and p-H_2CO based on observations with the IRAM 30 m toward the Horsehead PDR to estimate ortho-to-para ratios of around 3 at the dense core and 2 in the PDR. In a pioneering work, Mangum et al. (1990) stressed the importance of H_2CO as a key tracer to estimate density, temperature, and molecular abundances. They performed LTE and non-LTE calculations obtaining $n(H_2) = (0.5–1) \times 10^7$ cm^{-3} and $T_{kin} \approx 100$ K in Orion KL. In this work, we detect various lines of formaldehyde that were identified in Orion KL by Mangum et al. (1990).

3.2.3. Formyl Cation Isotopologues: LTE Analyses

The population diagram obtained for $H^{13}CO^+$ using the three detected lines is exhibited in Figure 7(d). Assuming that the emitting region is 5″, the excitation temperature and column density were estimated as $T_{exc} = 11 \pm 1$ K and $N = (2.1 \pm 0.7) \times 10^{14}$ cm^{-2} ($\chi^2_{red} = 1.30$), respectively. In the case of $HC^{18}O^+$ and $HC^{17}O^+$, no population diagram could be displayed because of the lack of enough detected lines. Nevertheless, LTE calculations were performed to estimate their column densities. Similar methodologies were discussed in Schöier et al. (2002), who performed LTE and non-LTE calculations for HCO^+ and its isotopologues in IRAS 16293–2422.

In this work, the LTE calculations of $HC^{18}O^+$ and $HC^{17}O^+$ were performed by fixing the excitation temperature to the value obtained for $H^{13}CO^+$ and considering the column densities as free parameters with the following condition: $N(HC^{17}O^+) < N(HC^{18}O^+) < N(H^{13}CO^+)$. The estimates of the column densities were $N(HC^{18}O^+) \approx 1.8 \times 10^{13}$ cm^{-2}

$(\chi^2_{red} = 1.5)$ and $N(HC^{17}O^+) \approx 1.4 \times 10^{13}$ cm^{-2} $(\chi^2_{red} = 0.3)$. Synthetic spectra are included in the panels of Figure 5.

The low temperature estimated from the H^{13}CO$^+$ lines suggests that its emission is likely associated with a cold and expanded region. In addition, we also obtained results assuming an extended source size of 15″. Thus, the H^{13}CO$^+$ population diagram gave the values $T_{exc} = 12 \pm 2$ K and $N = (2.6 \pm 0.8) \times 10^{13}$ cm^{-2}, and for the ^{18}O and ^{17}O isotopologues, it gave $N(HC^{18}O^+) \approx 4.2 \times 10^{12}$ and $N(HC^{17}O^+) \approx 1.5 \times 10^{12}$ cm^{-2}.

3.2.4. HCO$^+$: Non-LTE Calculations

The main isotopologue HCO$^+$ was observed through two intense and optically thick lines (Figure 4); they were analyzed via non-LTE calculations using collisional excitation rates. The two transitions, 2–1 and 3–2, were computed using RADEX and the rate coefficients available in the LAMDA database (Flower 1999) assuming $n(H_2) = (0.1–5) \times 10^7$ cm^{-3}, $T < 30$ K, and 5″. The column density resulted in $N(HCO^+) \approx 3 \times 10^{15}$ cm^{-2} $(\chi^2_{red} = 6.5)$. In the literature, line analysis of HCO$^+$ has been reported with high reduced values of χ^2 (Schöier et al. 2002). The result reported in this work should be taken as a rough approximation.

3.2.5. Protonated Formaldehyde: LTE Analysis

The three unblended lines of H$_2$COH$^+$ allowed us to obtain the population diagram shown in Figure 7(e) and the estimates $T_{exc} = 25 \pm 4$ K and $N = (1.4 \pm 0.3) \times 10^{14}$ cm^{-2} $(\chi^2_{red} = 0.41)$ assuming a source size of 5″. Figure 6 exhibits a comparison between the simulated and observed lines with the exception of the spectrum affected by contaminant emission.

In comparison with other works, Ohishi et al. (1996) reported $T_{exc} = 60–110$ K and $N(H_2COH^+) \approx 10^{12}–10^{14}$ cm^{-2} in surveys toward Sgr B2, Orion KL, and W51. In W51, since they could not detect a sufficient number of lines of H$_2$COH$^+$, they used HCO$^+$ to infer the physical conditions of H$_2$COH$^+$ taking different excitation temperatures. In the ultracold $(T \sim 10$ K) source L1689B, Bacmann et al. (2016) estimated column densities between 3×10^{11} and 1×10^{12} cm^{-2}. They discussed that the H$_2$COH$^+$ formation can occur via

$$H_2CO + x^+ \longrightarrow H_2COH^+ + H_2, \qquad (4)$$

where x$^+$ represents a proton donor such as H$_3^+$. Furthermore, in the context of Equation (1), the specific proton donor is HCO$^+$, obtaining CO as a by-product instead of H$_2$. They predicted the abundance ratios $[H_2COH^+] \approx 0.007[H_2CO]$ when H$_3^+$ is the proton donor and $[H_2COH^+] \approx 0.003 [H_2CO]$ when it is HCO$^+$.

In summary, we present in Table 3 the results obtained from the LTE and non-LTE analyses of the isotopologues of formaldehyde and the formyl cation. The results suggest that these species might trace different gas components. From the estimated column densities of the formaldehyde isotopologues, the abundance ratios H$_2$CO:H$_2^{13}$CO:HDCO:H$_2$C^{18}O $\approx$ 223:12:4:1 were obtained. In addition, Table 3 also presents the results obtained from the population diagram of H$_2$COH$^+$.

Table 3
Summary of the LTE and Non-LTE Analyses of the Isotopologues of Formaldehyde and the Formyl Cation and the Protonated Formaldehyde

Species	No. of Analyzed Lines	Method	N (cm^{-2}) $\approx$	T (K) $\approx$
H$_2$CO	9	Non-LTE[a]	1.52×10^{16}	91
H$_2^{13}$CO	13	LTE[b]	8.0×10^{14}	83
HDCO	8	LTE[b]	2.5×10^{14}	21
H$_2$C^{18}O	5	LTE[b]	6.8×10^{13}	31
D$_2$CO	2	LTE[c]	$<1.3 \times 10^{14}$	21
HCO$^+$	2	Non-LTE	3×10^{15}	<30
H^{13}CO$^+$	3	LTE[b]	2.1×10^{14}	11
HC^{18}O$^+$	2	LTE[d]	1.8×10^{13}	11
HC^{17}O$^+$	1	LTE[d]	1.4×10^{13}	11
H$_2$COH$^+$	3	LTE[b]	1.4×10^{14}	25

Notes. The temperatures and column densities come from the results obtained at a source size of 5″.
[a] From the o-H$_2$CO and p-H$_2$CO results, the column density and temperature are the sum and mean value, respectively.
[b] Obtained from the population diagram analysis.
[c] Upper limit based on the HDCO analysis.
[d] Obtained from the LTE calculation.

Table 4
Fractional Abundances of H$_2$CO, HCO$^+$, and H$_2$COH$^+$ in G331 in Comparison with Values Reported in Other Sources

Species	Fractional Abundances		
	This Work	Other Works	References
H$_2$CO	$(0.2–2) \times 10^{-8}$	$(2–8) \times 10^{-8}$	(1)
HCO$^+$	$(0.5–4) \times 10^{-9}$	2.3×10^{-9}	(2)
H$_2$COH$^+$	$(0.2–2) \times 10^{-10}$	$(0.01–1) \times 10^{-9}$	(3)

Note. (1) NGC 7129 FIRS 2 (Fuente et al. 2014). (2) OMC-1, extended ridge (Blake et al. 1987). (3) Sgr B2, Orion KL, and W51 (Ohishi et al. 1996).

4. Discussion

4.1. Fractional Abundances

The fractional abundances ($[X]$) were estimated with respect to molecular hydrogen using $[X] = N_i/N_{H_2}$, where N_i and N_{H_2} represent the column density of the species i and H$_2$, respectively. The H$_2$ column density was indirectly inferred from H^{13}CO$^+$ by means of the ratio H^{13}CO$^+$/H$_2 = 3.3 \times 10^{-11}$ (Blake et al. 1987; Merello et al. 2013; Sánchez-Monge et al. 2013). Using that ratio and the results obtained from the population diagrams of H^{13}CO$^+$, considering source sizes of 5″ and 15″, an interval of H$_2$ column densities was estimated as $N_{H_2} = (0.8–6) \times 10^{24}$ cm^{-2}. In the literature, similar H$_2$ column densities have been discussed in the context of high-mass star-forming regions (e.g., Motte et al. 2018; Yu et al. 2018). In addition, values of the order of $N_{H_2} \approx 10^{24}$ cm^{-2} have been used in Orion KL (e.g., Crockett et al. 2014). In Table 4, we summarize the abundances of the main isotopologues H$_2$CO, HCO$^+$, and H$_2$COH$^+$ obtained with respect to the estimated N_{H_2} interval and compared with values reported for the sources NGC 7129 FIRS 2, Orion KL, Sgr B2, and W51, which are sources known for exhibiting a rich chemistry in simple and complex organic molecules (Blake et al. 1986; Ohishi et al. 1996; Crockett et al. 2014; Fuente et al. 2014).
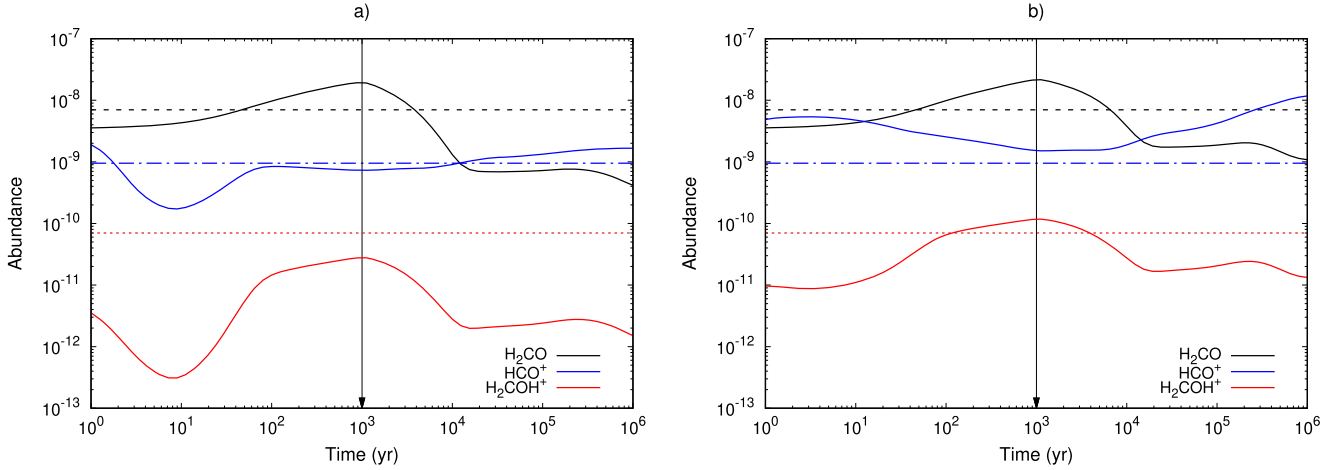
Figure 8. Predicted abundances of H_2CO, HCO^+, and H_2COH^+ as a function of time, represented by the black, blue, and red solid lines, respectively, obtained from a model with $T = 30$ K and $n_{H_2} = 1 \times 10^6$ cm^{-3}. Panel (a) represents a model with the whole chemical network, whereas panel (b) does not include the major destruction channels of HCO^+ and H_2COH^+. The dashed, dashed–dotted, and dotted horizontal lines indicate the mean fractional abundances observed in G331 for H_2CO, HCO^+, and H_2COH^+, respectively. The vertical line depicts the abundance peak of H_2CO at $t \approx 10^3$ yr.

4.2. Chemical Modeling

In the gas phase, there are several ion–molecule reactions that can explain the H_2COH^+ formation. In Equation (1), one of the most important mechanisms involving the chemical species H_2CO and HCO^+ is described (Tanner et al. 1979; Woon & Herbst 2009). Concerning surface reactions, Song & Kästner (2017) performed calculations about the hydrogenation of H_2CO in amorphous solid water surfaces and found some implications about the protonation of CH_3O isomers. The H_2COH^+ is a major product of the ionization and fragmentation of CH_3OH, CH_3CH_2OH, and CH_3OCH_3 (Mosley et al. 2012).

We observed that the reaction between H_2CO and HCO^+ is one of the most important channels to produce H_2COH^+, as well as the general scheme described in Equation (4). In addition, it is observed that other cations can also react with H_2CO to produce H_2COH^+, for instance,

$$H_2CO + H_3^+ \longrightarrow H_2COH^+ + H_2, \qquad (5)$$

$$H_2CO + H_3O^+ \longrightarrow H_2COH^+ + H_2O, \qquad (6)$$

and

$$H_2CO + N_2H^+ \longrightarrow H_2COH^+ + N_2, \qquad (7)$$

and the major reactions of destruction are

$$HCO^+ + e^- \longrightarrow CO + H, \qquad (8)$$

$$H_2COH^+ + e^- \longrightarrow HCO + 2H, \qquad (9)$$

and

$$H_2COH^+ + e^- \longrightarrow CO + H + H_2. \qquad (10)$$

In this work, we created a gas–grain model to study the chemistry of H_2CO, HCO^+, and H_2COH^+ (Section 2.1). As a result, the evolution of the gas abundances was simulated for these species. Therefore, we adopted the initial chemical abundances of Vidal & Wakelam (2018, and references therein) but considering the physical parameters obtained in this work from the line observations of H_2CO, HCO^+, and H_2COH^+ in G331. The model was computed using different values of gas temperature and density, assuming the ranges $T = 10$–90 K and $n_{H_2} = (0.05–1) \times 10^7$ cm^{-3}, respectively, and using a visual

extinction of $A_V = 10$ mag and a cosmic-ray ionization rate of $\zeta = 1.3 \times 10^{-17}$ cm^{-3}. The model that yielded the most accurate abundance prediction, consistent with the observed abundances within an order of magnitude, was obtained at $T = 30$ K and $n_{H_2} = 1 \times 10^6$ cm^{-3}. However, at temperatures and densities above these values, the model's chemistry becomes unpredictable. The result is exhibited in Figure 8, where we mark the mean values of the fractional abundances of H_2CO, HCO^+, and H_2COH^+ (given in Table 4) with horizontal lines (black dashed, blue dashed–dotted, and red dotted, respectively). Here it is observed that H_2CO reaches its maximum abundance at $\sim 10^3$ yr (the timescale of $\sim 10^3$ yr is indicated by a vertical line), in agreement with the results shown in Table 4. This timescale would be optimal for the formation of neutral species in G331. Furthermore, at a timescale of $\sim 10^2$–10^3 yr, the predicted abundances of HCO^+ and H_2COH^+ are in agreement with the observational mean values, in line with the general assumption of massive protostellar objects (i.e., young sources with an active chemistry with abundant molecular emission). These agreements make us develop the hypothesis that the lifetime of the source G331 might be $< 10^4$ yr.

To explore the effects of the major reactions of destruction, we carry out a second simulation, shown in Figure 8. While Figure 8(a) represents a model computed with the whole network of chemical reactions, Figure 8(b) depicts a model that excludes the destruction reactions described in Equations (8)–(10). In general, the major destructive reactions noticeably reduce the abundances of the molecular ions, but the abundance of neutral H_2CO remains relatively stable. In addition, in the models of Figures 8(a) and (b), it is observed that H_2COH^+ follows the abundance curves of HCO^+ and H_2CO, respectively. In the case of Figure 8(a), HCO^+ is a major precursor of H_2COH^+. Thus, changes in the abundance of HCO^+ affect the production of H_2COH^+. In the case of Figure 8(b), the increase of the abundance of HCO^+, which reacts with H_2CO to form H_2COH^+ (see Equation (1)), makes the abundance of H_2COH^+ rise.

The dissociative recombination of molecular ions with electrons is one of the most complex and destructive and least understood mechanisms in the ISM (Hamberg et al. 2007; Meier et al. 1993). Hamberg et al. (2007) carried out

experiments to measure the cross sections and branching ratios of various protonated and deuterated molecular ions. Meier et al. ([1993]) detected H_2COH^+ in the coma of the comet P/Halley and created an ion chemical model to estimate the H_2CO production from H_2COH^+. The chemical models presented in this work provide a preliminary framework for understanding the chemistry of molecular ions in cold regions of G331.

4.3. Isotopic Fractionation

D/H ratios. The ratio was calculated using the neutral isotopologues H_2CO and HDCO, while the molecular ions HCO^+ and DCO^+ were not used due to the nondetection of DCO^+ in G331. From the LTE and non-LTE analyses of HDCO and H_2CO, respectively, it is reported that HDCO/$H_2CO \sim 0.02$ for a bulk gas with $T < 90$ K and, from the D_2CO tentative detection, it was estimated that $D_2CO/H_2CO \leqslant 0.009$. Roberts & Millar ([2007]) estimated HDCO/$H_2CO \sim 0.01$, 0.03, and <0.002 in G34.26, G75.78, and G31.41, respectively. In addition, for the G34.26 and G75.78 sources, they also reported $D_2CO/H_2CO < 0.001$ and <0.01, respectively, for gas components within a broad distribution of temperatures ($T < 100$ K).

The HDCO detection demonstrated clear evidence of a deuteration fractionation in G331. In previous studies of G331 conducted with APEX, deuterated species were searched for, but no conclusive results were obtained (Mendoza et al. [2018]; Duronea et al. [2019]; Canelo et al. [2021]; Santos et al. [2022]).

$^{12}C/^{13}C$ ratios. The $H_2CO/H_2^{13}CO$ and $HCO^+/H^{13}CO^+$ ratios were estimated in G331 within ~ 14–20. Wilson & Rood ([1994]) analyzed isotopic carbon ratios from CO and H_2CO, reporting values of ~ 20 and 77 for the Galactic center and local ISM, respectively. Yan et al. ([2019]) estimated $^{12}C/^{13}C$ ratios from formaldehyde. From 112 observations, the transition $(1_{1,0}$–$1_{1,1})$ of H_2CO was detected in 84 sources, and of these 84, $H_2^{13}CO$ $(1_{1,0}$–$1_{1,1})$ was detected in 38 sources (the entire description is in Section 2 of Yan et al. [2019]). They found $^{12}C/^{13}C$ ratio values of up to 99 for the source G49.21–0.35, around 32 for G31.41+0.31, and ~ 16–47 for W31.

$^{16}O/^{18}O$ and $^{18}O/^{17}O$ ratios. The $H_2C^{16}O/H_2C^{18}O$ and $HC^{16}O^+/HC^{18}O^+$ ratios provided a rough estimate between ~ 170 and 250. In order to estimate the $^{18}O/^{17}O$ ratio from the integrated areas of the lines $HC^{17}O^+$ (2–1) and $HC^{18}O^+$ (2–1), the ratio $HC^{18}O^+/HC^{17}O^+ \sim 3$ is obtained, whose value represents an upper limit compared with the abundance ratio $HC^{18}O^+/HC^{17}O^+ \sim 1.3$ obtained for G331 from the LTE analysis. In the Galactic center and local ISM, Wilson & Rood ([1994]) obtained ratios of $^{16}O/^{18}O \sim 250$ and 560, respectively, as well as $^{18}O/^{17}O \sim 3.2$ for both of them. Persson et al. ([2018]) claimed the first detection of $H_2C^{17}O$ and $D_2^{13}CO$, among other isotopologues, in IRAS 16293–2422 B and reported the values $H_2C^{16}O/H_2C^{18}O \sim 800$, $H_2C^{16}O/H_2C^{17}O \sim 2596$, and $H_2C^{18}O/H_2C^{17}O \sim 3.2$.

In summary, we present in Table [5] the isotopic ratios estimated for G331 that are in good agreement compared to the values reported from GMCs (Orion, Sgr B2) and hot molecular cores such as G31.41 and G34.26 (Guelin et al. [1982]; Mangum et al. [1990]; Turner [1990]; Roberts & Millar [2007]; Neill et al. [2013]; Yan et al. [2019]).

Table 5
Ratios between the Isotopologues of H_2CO and HCO^+ Estimated for G331 that Are Compared with the Values Reported in GMCs, i.e., Orion and Sgr (B2), and Hot Molecular Cores (HMCs), i.e., G31.41 and G34.26

Ratios	G331	GMCs	G31.41	G34.26
Formaldehyde				
$H_2^{13}CO/H_2CO$	0.05	0.035[a]	0.03[e]	0.02[e]
HDCO/H_2CO	0.02	$\leqslant 0.005$[b]	<0.002[f]	0.01[f]
$D_2CO/HDCO$	$\lesssim 0.5$	0.02[c]	...	<0.001[f]
$H_2C^{18}O/H_2CO$	0.004	0.003[a]	...	...
Formyl cation				
$HCO^+/H^{13}CO^+$	14	21.2[d]	...	...
$HC^{18}O^+/HC^{17}O^+$	1.3	3.1[d]	...	...

Notes.
[a] Orion KL compact ridge (Mangum et al. [1990]).
[b] Orion KL hot core (Neill et al. [2013]).
[c] Orion KL compact ridge (Turner [1990]).
[d] Sgr B2 (Stark [1981]; Guelin et al. [1982]).
[e] HMCs (Yan et al. [2019]).
[f] HMCs (Roberts & Millar [2007]).

5. Conclusions and Perspectives

We have identified isotopologues of formaldehyde, the formyl cation, and protonated formaldehyde in G331, a hot molecular core and outflow system. The search for these species was carried out using spectral setups collected with the APEX telescope in a frequency range of ~ 159–356 GHz. A time-dependent chemical model using the gas–grain code NAUTILUS was created to study the chemistry and predict the abundances of H_2CO, HCO^+, and H_2COH^+ as a function of time. The conclusions and perspectives are as follows.

1. Formaldehyde is an abundant molecule in G331. Several lines of H_2CO, $H_2^{13}CO$, HDCO, and $H_2C^{18}O$ were detected in G331, 35 spectral lines in total. The D_2CO was tentatively detected and used to set an upper threshold for its abundance. From non-LTE calculations, the o- and p-H_2CO spectral lines provided kinetic temperatures between ~ 87 and 95 K. From the population diagrams assuming the LTE approximation, the spectral lines of $H_2^{13}CO$, HDCO, and $H_2C^{18}O$ provided excitation temperatures of ~ 83, 21, and 31 K. From the estimates of column densities considering a source size of $5''$, the ratios $H_2CO:H_2^{13}CO:HDCO:H_2C^{18}O \approx 223:12:4:1$ were obtained. The formaldehyde isotopologues can trace different physical conditions, from cold gas to lukewarm temperatures. These results agree with sublimation processes and the active gas–grain chemistry expected in hot molecular cores.

2. The formyl cation is also an abundant species in G331. In total, eight rotational lines of HCO^+, $H^{13}CO^+$, $HC^{18}O^+$, and $HC^{17}O^+$ were identified in G331. In contrast with formaldehyde, the ^{17}O isotopologue, $HC^{17}O^+$, was detected, but the deuterated one, DCO^+, was not. Assuming the LTE approximation, the population diagram of $H^{13}CO^+$ provided a temperature and column density $T_{exc} \approx 11$ K and $N(H^{13}CO^+) \approx 2.1 \times 10^{14}$ cm^{-2}, whose values were used to estimate the column densities of $HC^{18}O^+$ and $HC^{17}O^+$. From non-LTE calculations, the spectral lines of HCO^+ provided $N(HCO^+) \approx 3 \times 10^{15}$ cm^{-2} assuming a temperature of about 30 K.

3. Protonated formaldehyde, H_2COH^+, should be present under interstellar conditions when H_2CO and HCO^+ are detected (see Equation (1)). In fact, this cation was also detected through four lines, one of which is likely blended with $^{34}SO_2$. From the population diagram considering the LTE formalism, $T_{exc} \approx 25$ K and $N(H_2COH^+) \approx 1.4 \times 10^{14}$ cm^{-2} was obtained adopting a source size of 5″. The H_2CO and HCO^+ can produce H_2COH^+ under interstellar conditions. In addition, these species could play a key role in the formation of complex organic molecules.

4. A gas–grain chemical model was created to predict the fractional abundances of H_2CO, HCO^+, and H_2COH^+ and study their evolution. The best model was obtained adopting $T = 30$ K and $n_{H_2} = 1 \times 10^6$ cm^{-3}. In a young molecular stage of $\sim 10^5$ yr, the H_2CO, HCO^+, and H_2COH^+ abundances reached values comparable to those derived from the observations, $[H_2CO] = (0.2–2) \times 10^{-8}$, $[HCO^+] = (0.5–4) \times 10^{-9}$, and $[H_2COH^+] = (0.2–2) \times 10^{-10}$. The reaction between H_2CO and HCO^+ is one of the major channels to produce H_2COH^+. On the other hand, it was noticed that dissociative recombination mechanisms with electrons can rapidly destroy HCO^+ and H_2COH^+, affecting their predicted abundances. The results obtained with the chemical modeling of the three molecular species make us develop a hypothesis that the evolutionary stage of

5. From the multiline analysis of formaldehyde and the formyl cation, new $^{12}C/^{13}C$, H/D, $^{16}O/^{18}O$, and $^{18}O/^{17}O$ ratios were inferred in G331 and agree with the results of other works. In particular, deuterium was observed in formaldehyde but not in the formyl cation, HDCO, and DCO^+. The ^{17}O was observed in the formyl cation but not in formaldehyde, $HC^{17}O^+$, and $H_2C^{17}O$. In perspective, along with a new observational analysis, gas–grain chemical models might shed light on the molecular processes that lead different isotopic ratios.

Appendix
Update of the Internal Partition Functions of the Detected Isotopologues of Formaldehyde

The internal partition functions of the isotopologues of formaldehyde $H_2^{13}CO$, $H_2C^{18}O$, HDCO, and D_2CO detected in this work have been updated. Since the lists of energies, either experimental or theoretical, of the rovibrational levels for these isotopologues are incomplete for computing the internal partition functions for temperatures up to 500 K, the direct sum expression does not reach the convergence. Therefore, the internal partition functions of the isotopologues of formaldehyde have to be computed using some other tested approximations (Carvajal et al. 2019), e.g., writing it in terms of the product of the rotational contribution ($Q_{rot}(T)$) and the harmonic approximation of the vibrational contribution ($Q_{vib}^{harm}(T)$; Herzberg 1991),

$$Q_{rv}(T) \approx Q_{rot}(T) \, Q_{vib}^{harm}(T) \ , \qquad (A1)$$

where the rotational contribution $Q_{rot}(T)$ is computed as a direct sum (e.g., Herzberg 1991) because there are enough rotational energies for the typical temperatures of the ISM,

$$Q_{rot}(T) = \sum_i g_{ns}^{(i)} \, (2 J_i + 1) \, e^{-\frac{E_i^{(rot)}}{kT}} \ , \qquad (A2)$$

where $E_i^{(rot)}$ represents the energy for the ith rotational state in the ground vibrational state assuming that the ground electronic state is uniquely populated. The rotational energies of the isotopologues of formaldehyde have been taken from the CDMS (Endres et al. 2016) and JPL (Pickett et al. 1998).

The nuclear spin degeneracy $g_{ns}^{(i)}$ is included in the definition of the rotational contribution of the partition function (Equation (A2)) because, in general, the values of $g_{ns}^{(i)}$ can be different depending on the symmetry of the rotational states. In the case of formaldehyde, the isotopologues $H_2^{13}CO$, $H_2C^{18}O$, and D_2CO have symmetry $\mathcal{C}_{2v}(M)$, whose rovibrational states are characterized by the irreducible representations A_1, A_2, B_1, and B_2, whereas the monodeuterated isotopologue HDCO has symmetry $\mathcal{C}_s(M)$, and its states are labeled with the irreducible representations A' and A'' (Bunker & Jensen 1989). The labelings of the rotational states of the different isotopologues and their nuclear spin statistical weights are given in Table 6.

Although the validity of the approximation (Equation (A1)) has been proven suitable for the typical ISM temperatures (Carvajal et al. 2019), a new check is carried out comparing the values of the internal partition function of the main isotopologue of formaldehyde from 2.725 to 500 K with those calculated as a direct sum of a comprehensive data set for the rovibrational energy levels provided by Al-Refaie et al. (2015). In Table 7, the values of the harmonic approximation for the vibrational partition function $Q_{vib}^{harm}(T)$ and the internal partition function $Q_{rv}(T)$ (Equation (A1)) for the main isotopologue are given. The $Q_{vib}^{harm}(T)$ is calculated using the experimental fundamental vibrational energies taken from Perrin et al. (2003, 2006), and the rotational partition function is computed from the JPL rotational energies predicted up to $J = 99$ and $K_a = 25$ (Pickett et al. 1998). The uncertainties of the rovibrational partition function (Carvajal et al. 2019) are obtained considering the uncertainties of all of the rotational energies provided in the JPL database (Pickett et al. 1998) and the experimental uncertainties of the vibrational fundamental energies (Perrin et al. 2003, 2006).

Table 6
Nuclear Spin Statistical Weights of the Isotopologues of Formaldehyde H_2CO, $H_2^{13}CO$, $H_2C^{18}O$, D_2CO, and HDCO Associated with the Rotational States[a]

Isotopologues	Γ_{rot}[b]	K_a[c]	K_c[c]	$g_{ns}^{(i)}$	Type[g]
H_2CO, $H_2C^{18}O$	A_1	Even	Even	1	para
	A_2	Even	Odd	1	para
	B_1	Odd	Odd	3	ortho
	B_2	Odd	Even	3	ortho
$H_2^{13}CO$	A_1	Even	Even	2[d]	para
	A_2	Even	Odd	2[d]	para
	B_1	Odd	Odd	6[d]	ortho
	B_2	Odd	Even	6[d]	ortho
D_2CO	A_1	Even	Even	6[e]	ortho
	A_2	Even	Odd	6[e]	ortho
	B_1	Odd	Odd	3[e]	para
	B_2	Odd	Even	3[e]	para
HDCO	A'	⋯	Even	6[f]	⋯
	A''	⋯	Odd	6[f]	⋯

Notes.
[a] The nuclear spin degeneracy $g_{ns}^{(i)}$ is computed according to Bunker & Jensen (1989).
[b] The symmetry labeling of the rotational states.
[c] The rotational states of the asymmetric top, such as formaldehyde, are labeled by the quantum numbers J_{K_a,K_c}, where J is the rotational angular momentum, and K_a and K_c are the projections of the rotational angular momentum along the a- and c-molecule-fixed axes. In this case, the symmetry of the rotational states is characterized by their even and odd values of K_a and K_c. For the monodeuterated isotopologue, the two symmetries are only characterized by the even and odd values of K_c.
[d] For $H_2^{13}CO$, the nuclear spin degeneracy is also considered in the literature with a ratio of 3:1 for the ortho:para states (see, e.g., Endres et al. 2016). As a warning in order to avoid wrong results, before using data from a catalog, it should be checked whether the nuclear spin weights agree with the partition function considered.
[e] For D_2CO, the nuclear spin degeneracy is also considered in the literature with a ratio of 2:1 (ortho:para; see, e.g., Endres et al. 2016). The same warning from footnote d should be considered in this case.
[f] For the monodeuterated isotopologue, the nuclear spin degeneracy is considered in this paper as 1 because the degeneracy is state-independent.
[g] Only for the symmetric isotopologues of formaldehyde, this column shows whether the transitions involving these rotational states are ortho or para.

These values are compared with those from the CDMS catalog (Endres et al. 2016) and Al-Refaie et al. (2015). According to the relative differences between the approximated internal partition function (Equation (A1)) and the one calculated more thoroughly (Al-Refaie et al. 2015), the two results are comparable in the temperature interval from 2.725 to 500 K. However, the difference from the values provided in the CDMS catalog is −8.8% at 500 K and −0.72% at 300 K. Therefore, as the approximation (Equation (A1)) using a harmonic vibrational partition function is acceptable for the interval of temperature typical for the ISM and notably improves the values of the JPL and CDMS catalogs for higher temperatures, this is going to be used for the other isotopologues of formaldehyde.

Table 8 evinces the values of the partition function of $H_2^{13}CO$, $H_2C^{18}O$, D_2CO, and HDCO calculated in this work. As in Table 7, the values of the calculated partition function are compared with those available in the CDMS database (Endres et al. 2016). For the case of $H_2^{13}CO$, the values and uncertainties of $Q_{rv}(T)$ are computed using experimental fundamental vibrational energies (Ng & Tan 2017; Wohar & Jagodzinski 1991) for the harmonic partition function and rotational energies up to $J = 99$ and $K_a = 25$ taken from the JPL database (Pickett et al. 1998). The highest relative difference between this work and the CDMS values is −0.76% at $T = 300$ K. Therefore, at this temperature, it is not relevant to incorporate the vibrational contribution to the partition function. Nevertheless, the vibrational contribution is important at $T = 500$ K, increasing the rotational partition function by about 9%.

For the isotopologue $H_2C^{18}O$, only the values of the rotational partition function are evinced in Table 8. These values and their uncertainties have been calculated using the CDMS rotational data (up to $J = 54$, $K_a = 16$) complemented with those predicted for the excited rotational levels from the JPL database (up to $J = 20$, $K_a = 20$) when missing in the CDMS catalog. The vibrational partition function could not be calculated because, as far as we know, there are neither fundamental nor excited vibrational energies reported in the literature at all. This hindrance could be overcome provided that the vibrational fundamental energies are calculated by ab initio or other empirical approaches. Therefore, the partition

Table 7
Vibrational and Rovibrational Partition Function of the Main Isotopologue of Formaldehyde (H_2CO)

T (K)	Q_{vib}^{harm}[b]	Q_{rv} (Present Work)[c]	Q (CDMS)[d]	Q (Al-Refaie et al. 2015)[e]	Rel. Diff.(%)[f]
2.725	1.000000	2.0166(0)	2.0166	2.0165	0.00
5.000	1.000000	4.4832(0)	4.4832	4.4833	0.00
9.375	1.000000	13.8009(0)	13.8008	13.8010	0.00
18.750	1.000000	44.6813(0)	44.6812	44.6835	0.00
37.500	1.000000	128.6496(0)	128.6492	128.6581	0.01
75.000	1.000000	361.7207(0)	361.7195	361.7053	0.00
150.000	1.000021	1019.9947(0)	1019.9706	1019.9549	0.00
225.000	1.000996	1874.4927(0)	1872.6221	1874.4679	0.00
300.000	1.007228	2903.8609(0)	2883.0163	2904.1778	0.01
500.000	1.087521	6751.7086(3)	6208.3442	6760.2315	0.13

Notes. Comparison between the values obtained in the present study and those published before.[a]
[a] The nuclear spin degeneracy is given in Table 6.
[b] Values of the vibrational partition function computed with the harmonic approximation. For more details, see the text.
[c] $Q_{rv} = Q_{rot}$(direct sum) Q_{vib}^{harm}. An estimate of the uncertainties is given in parentheses in units of the last quoted digits. For more details, see the text.
[d] Rotational partition function computed as a direct sum with no vibrational contribution. Their values are reported in the CDMS catalog (Endres et al. 2016).
[e] Internal partition function computed as the direct sum using a comprehensive set of rovibrational energies up to 18,000 cm^{-1} and $J = 70$ (Al-Refaie et al. 2015).
[f] Relative difference of the partition function computed in the present study with respect to the one reported by Al-Refaie et al. (2015).

Table 8
Vibrational and Rovibrational Partition Functions for the Isotopologues $H_2^{13}CO$, $H_2C^{18}O$, D_2CO, and HDCO

	$H_2^{13}CO$				$H_2C^{18}O$		
T (K)	$Q_{vib}^{harm\,b}$	Q_{rv} (Present Work)[c]	Q (CDMS)[d]	Rel. Diff.(%)[e]	Q_{rot} (Present Work)[c]	Q (CDMS)[d]	Rel. Diff.(%)[e]
2.725	1.000000	4.1136(0)	4.1136	0.00	2.0944(0)	2.0944	0.00
5.0	1.000000	9.1701(0)	9.1700	0.00	4.6806(0)	4.6805	0.00
9.375	1.000000	28.2638(0)	28.2636	0.00	14.4425(0)	14.4424	0.00
18.75	1.000000	91.5675(0)	91.5672	0.00	46.8159(0)	46.8156	0.00
37.50	1.000000	263.7391(0)	263.7382	0.00	134.8810(0)	134.8805	0.00
75.0	1.000000	741.6749(0)	741.6726	0.00	379.3628(0)	379.3616	0.00
150.0	1.000023	2091.5874(3)	2091.5330	0.00	1069.8884(0)	1069.8850	0.00
225.0	1.001065	3844.176(18)	3840.0722	−0.11	1964.3668(0)	1964.3606	0.00
300.0	1.007605	5957.09(14)	5912.1084	−0.76	3024.3241(1)	3024.3231	0.00
500.0	1.090530	13884.1(19)	…	…	6508.862(13)	…	…

	D_2CO				HDCO			
T (K)	$Q_{vib}^{harm\,b}$	Q_{rv} (Present Work)[c]	Q (CDMS)[d]	Rel. Diff.(%)[e]	$Q_{vib}^{harm\,b}$	Q_{rv} (Present Work)[c]	Q (CDMS)[d]	Rel. Diff.(%)[e]
2.725	1.000000	14.984964(0)	14.9850	0.00	1.000000	2.2608(0)	2.2608	0.00
5.000	1.000000	29.703636(0)	29.7036	0.00	1.000000	4.6483(0)	4.6483	0.00
9.375	1.000000	67.339744(0)	67.3395	0.00	1.000000	11.2681(0)	11.2680	0.00
18.750	1.000000	182.210324(0)	182.2098	0.00	1.000000	31.0556(0)	31.0555	0.00
37.500	1.000000	509.265756(0)	509.2641	0.00	1.000000	86.7359(0)	86.7356	0.00
75.000	1.000000	1432.775532(0)	1432.7709	0.00	1.000000	243.8496(0)	243.8488	0.00
150.000	1.000226	4044.511598(0)	4043.5866	0.02	1.000093	688.0292(0)	687.9631	−0.01
225.000	1.005192	7464.6706(1)	7426.0941	−0.52	1.002701	1266.752(29)	1263.3349	−0.27
300.000	1.025736	11729.1102(6)	11434.7820	−2.57	1.015159	1974.73(18)	1945.2333	−1.52
500.000	1.202824	29624.2096(74)	…	…	1.138623	4769.8(21)	…	…

Notes. Comparison between the values obtained in the present study and those published in the CDMS catalog.[a]
[a] The nuclear spin degeneracy is considered according to Table 6.
[b] The vibrational partition function is computed with the harmonic approximation. For more details, see the text.
[c] $Q_{rv} = Q_{rot}$(direct sum) Q_{vib}^{harm}. An upward estimate of the uncertainties is given in parentheses in units of the last quoted digits. For more details, see the text. For the isotopologue $H_2C^{18}O$, the rotational partition function is presented because there are neither experimental nor theoretical vibrational levels available in the literature.
[d] Rotational partition function computed as a direct sum with no vibrational contribution. Their values are reported in the CDMS catalog (Endres et al. 2016). The CDMS partition functions of $H_2^{13}CO$ and D_2CO are multiplied by 2 and 3, respectively, to consider the same nuclear spin statistical weight from Table 6.
[e] Relative difference of the partition function given in the present study with respect to the one reported in the CDMS catalog.

function in the present work is practically the same as that reported in the CDMS, apart from the uncertainties and the new values of the rotational partition function for temperatures from 300 to 500 K.

The vibrational and internal partition functions of the double deuterated isotopologue D_2CO are presented in Table 8. The vibrational contribution and its uncertainty have been calculated using the available experimental vibrational fundamental bands (Perrin et al. 1998; Lohilahti & Alanko 2001; Lohilahti et al. 2006). The values and uncertainties of the rotational partition function are calculated using the CDMS rotational energies (with data up to $J = 66$ and $K_a = 26$) complemented by the higher excited rotational energy predictions (up to $J = 60$ and $K_a = 60$) given in the JPL database. At $T = 300$ K, the difference of the updated internal partition function from the CDMS values is around 2.6%, and this will be around 20% at $T = 500$ K.

The values and uncertainties of the internal partition function of the monodeuterated isotopologue HDCO, as well as the vibrational contribution, are also included in Table 8. The values of the rotational partition function are calculated using the CDMS rotational energies (up to $J = 56$ and $K_a = 20$) complemented by JPL higher excited rotational energy predictions up to $J = 90$ and $K_a = 50$. Since the CDMS data are more accurate, they were substituted in the JPL predictions to have a more accurate internal partition function. The vibrational partition function is computed using the available experimental and calculated fundamental energies (Oka & Morino 1961; Dangoisse et al. 1978; Ellsworth et al. 2008; Morgan et al. 2018). The experimental uncertainties of the fundamentals ν_1, ν_2, ν_4, and ν_6 measured by dispersed fluorescence spectroscopy (Ellsworth et al. 2008) are considered to be $2\,cm^{-1}$ according to the widths of the spectral lines, whereas the uncertainties of the ν_3 and ν_5 bands obtained with Discrete Variable Representation (DVR) calculations are assigned $1.20\,cm^{-1}$. By comparing with the CDMS data, the relative difference of the updated internal partition function is 1.5% larger at $T = 300$ K and at least 14% at $T = 500$ K.

In general, the updates of the internal partition functions incorporate the vibrational contribution, as well as the uncertainties and new values from 300 to 500 K for the four isotopologues $H_2^{13}CO$, $H_2C^{18}O$, D_2CO, and HDCO. As supplementary material, their rotational, vibrational, and rovibrational partition functions are reported up to $T = 500$ K using a 1 K interval. This update of the partition functions could be relevant for the estimate of the abundances of the four isotopologues of formaldehyde.

ORCID iDs

Edgar Mendoza https://orcid.org/0000-0001-9381-7826
Miguel Carvajal https://orcid.org/0000-0001-8743-129X
Leonardo Bronfman https://orcid.org/0000-0002-9574-8454

Heloisa M. Boechat-Roberty ⓞ https://orcid.org/0000-0001-8246-4842

References

Al-Refaie, A. F., Yachmenev, A., Tennyson, J., & Yurchenko, S. N. 2015, MNRAS, 448, 1704

Araya, E. D., Olmi, L., Morales Ortiz, J., et al. 2015, ApJS, 221, 10

Bacmann, A., García-García, E., & Faure, A. 2016, A&A, 588, L8

Bacmann, A., Lefloch, B., Ceccarelli, C., et al. 2003, ApJL, 585, L55

Belitsky, V., Lapkin, I., Fredrixon, M., et al. 2018, A&A, 612, A23

Bianchi, E., Codella, C., Ceccarelli, C., et al. 2017, MNRAS, 467, 3011

Blake, G. A., Sutton, E. C., Masson, C. R., & Phillips, T. G. 1986, ApJS, 60, 357

Blake, G. A., Sutton, E. C., Masson, C. R., & Phillips, T. G. 1987, ApJ, 315, 621

Bronfman, L., Garay, G., Merello, M., et al. 2008, ApJ, 672, 391

Bunker, P. R., & Jensen, P. 1989, Molecular Symmetry and Spectroscopy (Ottawa: NRC Research Press)

Canelo, C. M., Bronfman, L., Mendoza, E., et al. 2021, MNRAS, 504, 4428

Carvajal, M., Favre, C., Kleiner, I., et al. 2019, A&A, 627, A65

Ceccarelli, C., Castets, A., Loinard, L., Caux, E., & Tielens, A. G. G. M. 1998, A&A, 338, L43

Chapovsky, P. 2001, JMoSt, 599, 337

Clouthier, D. J., & Ramsay, D. A. 1983, ARPC, 34, 31

Crockett, N. R., Bergin, E. A., Neill, J. L., et al. 2014, ApJ, 781, 114

Dangoisse, D., Willemot, E., & Bellet, J. 1978, JMoSp, 71, 414

Dumke, M., & Mac-Auliffe, F. 2010, Proc. SPIE, 7737, 77371J

Duronea, N. U., Bronfman, L., Mendoza, E., et al. 2019, MNRAS, 489, 1519

Eckhardt, A. K., Linden, M. M., Wende, R. C., Bernhardt, B., & Schreiner, P. R. 2018, NatCh, 10, 1141

Ellsworth, K. K., Lajiness, B. D., Lajiness, J. P., & Polik, W. F. 2008, JMoSp, 252, 205

Endres, C. P., Schlemmer, S., Schilke, P., Stutzki, J., & Müller, H. S. P. 2016, JMoSp, 327, 95

Féraud, G., Bertin, M., Romanzin, C., et al. 2019, ECS, 3, 1135

Ferus, M., Pietrucci, F., Saitta, A. M., et al. 2019, A&A, 626, A52

Flower, D. R. 1999, MNRAS, 305, 651

Ford, K. E. S., Neufeld, D. A., Schilke, P., & Melnick, G. J. 2004, ApJ, 614, 990

Fuente, A., Cernicharo, J., Caselli, P., et al. 2014, A&A, 568, A65

Gardner, F. F., & Whiteoak, J. B. 1974, Natur, 247, 526

Ghesquière, P., Mineva, T., Talbi, D., et al. 2015, PCCP, 17, 11455

Goldsmith, P. F., & Langer, W. D. 1999, ApJ, 517, 209

Guelin, M., Cernicharo, J., & Linke, R. A. 1982, ApJL, 263, L89

Güsten, R., Nyman, L. Å, Schilke, P., et al. 2006, A&A, 454, L13

Guzmán, V. V., Goicoechea, J. R., Pety, J., et al. 2013, A&A, 560, A73

Halfen, D. T., Apponi, A. J., Woolf, N., Polt, R., & Ziurys, L. M. 2006, ApJ, 639, 237

Hamberg, M., Geppert, W. D., Thomas, R. D., et al. 2007, MolPh, 105, 899

Hasegawa, T. I., & Herbst, E. 1993, MNRAS, 263, 589

Helmich, F. P., & van Dishoeck, E. F. 1997, A&AS, 124, 205

Hervías-Caimapo, C., Merello, M., Bronfman, L., et al. 2019, ApJ, 872, 200

Herzberg, G. 1991, Spectra and Molecular Structure: II. Infrared and Raman Spectra of Polyatomic Molecules (Florida: Krieger Pub. Co., Malabar)

Horn, A., Møllendal, H., Sekiguchi, O., et al. 2004, ApJ, 611, 605

Jewell, P. R., Hollis, J. M., Lovas, F. J., & Snyder, L. E. 1989, ApJS, 70, 833

Kalvāns, J. 2021, ApJ, 910, 54

Lacy, J. H., Knacke, R., Geballe, T. R., & Tokunaga, A. T. 1994, ApJL, 428, L69

Layssac, Y., Gutiérrez-Quintanilla, A., Chiavassa, T., & Duvernay, F. 2020, MNRAS, 496, 5292

Lohilahti, J., & Alanko, S. 2001, JMoSp, 205, 248

Lohilahti, J., Ulenikov, O., Bekhtereva, E., Alanko, S., & Anttila, R. 2006, JMoSt, 780, 182

Loren, R. B. 1984, Technical Report, AST 8116403-1

Mangum, J. G., & Shirley, Y. L. 2015, PASP, 127, 266

Mangum, J. G., Wootten, A., Loren, R. B., & Wadiak, E. J. 1990, ApJ, 348, 542

Maret, S., Ceccarelli, C., Caux, E., et al. 2004, A&A, 416, 577

Maret, S., Hily-Blant, P., Pety, J., Bardeau, S., & Reynier, E. 2011, A&A, 526, A47

Martín-Doménech, R., Bergner, J. B., Öberg, K. I., & Jørgensen, J. K. 2019, ApJ, 880, 130

Meier, R., Eberhardt, P., Krankowsky, D., & Hodges, R. R. 1993, A&A, 277, 677

Mendoza, E., Bronfman, L., Duronea, N. U., et al. 2018, ApJ, 853, 152

Merello, M., Bronfman, L., Garay, G., et al. 2013, ApJL, 774, L7

Morgan, W. J., Matthews, D. A., Ringholm, M., et al. 2018, JCTC, 14, 1333

Mosley, J. D., Cheng, T. C., & Duncan, M. A. 2012, in 67th OSU Int. Symp. Molecular Spectroscopy (Columbus, OH: Ohio State Univ.)

Motte, F., Bontemps, S., & Louvet, F. 2018, ARA&A, 56, 41

Muders, D., Hafok, H., Wyrowski, F., et al. 2006, A&A, 454, L25

Müller, H. S. P., & Lewen, F. 2017, JMoSp, 331, 28

Neill, J. L., Crockett, N. R., Bergin, E. A., Pearson, J. C., & Xu, L.-H. 2013, ApJ, 777, 85

Ng, L., & Tan, T. 2017, JMoSp, 331, 82

Ohishi, M., Ishikawa, S.-I., Amano, T., et al. 1996, ApJL, 471, L61

Oka, T., & Morino, Y. 1961, JPSJ, 16, 1235

Osterbrock, D. E. 1962, ApJ, 136, 359

Pagani, L., Lesaffre, P., Jorfi, M., et al. 2013, A&A, 551, A38

Paiva, M. A. M., Pilling, S., Mendoza, E., Galvão, B. R. L., & De Abreu, H. A. 2023, MNRAS, 519, 2518

Pegues, J., Öberg, K. I., Bergner, J. B., et al. 2020, ApJ, 890, 142

Perrin, A., Flaud, J.-M., Predoi-Cross, A., et al. 1998, JMoSp, 187, 61

Perrin, A., Keller, F., & Flaud, J.-M. 2003, JMoSp, 221, 192

Perrin, A., Valentin, A., & Daumont, L. 2006, JMoSt, 780, 28

Persson, M. V., Jørgensen, J. K., Müller, H. S. P., et al. 2018, A&A, 610, A54

Pickett, H. M., Poynter, R. L., Cohen, E. A., et al. 1998, J. Quant. Spec. Radiat. Transf., 60, 883

Pratap, P., Menten, K. M., & Snyder, L. E. 1994, ApJL, 430, L129

Quénard, D., Bottinelli, S., & Caux, E. 2017, MNRAS, 468, 685

Reboussin, L., Wakelam, V., Guilloteau, S., & Hersant, F. 2014, MNRAS, 440, 3557

Roberts, H., & Millar, T. J. 2007, A&A, 471, 849

Roueff, A., Gerin, M., Gratier, P., et al. 2021, A&A, 645, A26

Ruaud, M., Loison, J. C., Hickson, K. M., et al. 2015, MNRAS, 447, 4004

Ruaud, M., Wakelam, V., & Hersant, F. 2016, MNRAS, 459, 3756

Sahu, D., Minh, Y. C., Lee, C.-F., et al. 2018, MNRAS, 475, 5322

Sánchez-Monge, Á, López-Sepulcre, A., Cesaroni, R., et al. 2013, A&A, 557, A94

Santos, J. C., Bronfman, L., Mendoza, E., et al. 2022, ApJ, 925, 3

Schöier, F. L., Jørgensen, J. K., van Dishoeck, E. F., & Blake, G. A. 2002, A&A, 390, 1001

Schutte, W. A., Gerakines, P. A., Geballe, T. R., van Dishoeck, E. F., & Greenberg, J. M. 1996, A&A, 309, 633

Semenov, D., Hersant, F., Wakelam, V., et al. 2010, A&A, 522, A42

Shimonishi, T., Onaka, T., Kawamura, A., & Aikawa, Y. 2016, ApJ, 827, 72

Singh, S. K., Fabian Kleimeier, N., Eckhardt, A. K., & Kaiser, R. I. 2022, ApJ, 941, 103

Snyder, L. E., Buhl, D., Zuckerman, B., & Palmer, P. 1969, PhRvL, 22, 679

Song, L., & Kästner, J. 2017, ApJ, 850, 118

Stark, A. A. 1981, ApJ, 245, 99

Sutton, E. C., Peng, R., Danchi, W. C., et al. 1995, ApJS, 97, 455

Tang, X. D., Henkel, C., Menten, K. M., et al. 2021, A&A, 655, A12

Taniguchi, K., Guzmán, A. E., Majumdar, L., Saito, M., & Tokuda, K. 2020, ApJ, 898, 54

Taniguchi, K., Saito, M., Majumdar, L., et al. 2018, ApJ, 866, 150

Tanner, S. D., Mackay, G. I., & Bohme, D. K. 1979, CaJCh, 57, 2350

Troscompt, N., Faure, A., Wiesenfeld, L., Ceccarelli, C., & Valiron, P. 2009, A&A, 493, 687

Tsuge, M., Hidaka, H., Kouchi, A., & Watanabe, N. 2020, ApJ, 900, 187

Turner, B. E. 1990, ApJL, 362, L29

van der Tak, F. F. S., Black, J. H., Schöier, F. L., Jansen, D. J., & van Dishoeck, E. F. 2007, A&A, 468, 627

Vassilev, V., Meledin, D., Lapkin, I., et al. 2008, A&A, 490, 1157

Vastel, C., Bottinelli, S., Caux, E., Glorian, J. M., & Boiziot, M. 2015, in SF2A-2015: Proc. of the Annual meeting of the French Society of Astronomy and Astrophysics, ed. F. Martins et al. (Toulouse: SF2A), 313

Vidal, T. H. G., & Wakelam, V. 2018, MNRAS, 474, 5575

Wakelam, V., Loison, J. C., Herbst, E., et al. 2015, ApJS, 217, 20

Watanabe, N., Shiraki, T., & Kouchi, A. 2003, ApJL, 588, L121

Wiesenfeld, L., & Faure, A. 2013, MNRAS, 432, 2573

Wilson, T. L., & Rood, R. 1994, ARA&A, 32, 191

Wohar, M. M., & Jagodzinski, P. W. 1991, JMoSp, 148, 13

Woods, P. M., Kelly, G., Viti, S., et al. 2012, ApJ, 750, 19

Woon, D. E., & Herbst, E. 2009, ApJS, 185, 273

Wootten, A., Loren, R. B., & Bally, J. 1984, ApJ, 277, 189

Yan, Y. T., Zhang, J. S., Henkel, C., et al. 2019, ApJ, 877, 154

Yu, N.-P., Xu, J.-L., Wang, J.-J., & Liu, X.-L. 2018, ApJ, 865, 135

Zapata, L. A., Schmid-Burgk, J., & Menten, K. M. 2011, A&A, 529, A24